

Unified Integer and Fractional Quantum Hall Effects from Boundary-Induced Edge-State Quantization

Pedro Pereyra

Departamento de Ciencias Básicas, UAM-Azcapotzalco, México D.F., C. P. 02200, México

(Dated: March 20, 2026)

Despite the success of Landau-level theory and edge-state transport formalisms, a direct microscopic link between bulk quantization and the experimentally observed hierarchy of quantum Hall plateaus has not been established. In particular, no unified microscopic mechanism accounting simultaneously for integer and fractional sequences has been derived within standard quantum mechanics.

Here we show that boundary-induced quantization of edge states provides this missing bridge. Starting from the Landau problem in laterally confined two-dimensional electron systems, we demonstrate that the imposition of Dirichlet, Neumann, and mixed (Robin) boundary conditions discretizes both the guiding-center coordinate and the longitudinal momentum of chiral edge states. The resulting boundary-dependent spectra generate families of edge channels with well-defined multiplicities that couple directly to electronic transport.

When incorporated into an edge-state transport description, this boundary quantization reproduces the integer Hall sequence and simultaneously yields a structured hierarchy of fractional filling factors without invoking separate microscopic mechanisms. We further show that a weak Hall-induced parity-breaking contribution reorganizes the low-energy edge spectrum while leaving the bulk Landau levels intact. This controlled symmetry breaking enhances edge-state multiplicities at small Landau indices and stabilizes the fractional plateaus observed at strong magnetic fields.

The quantized Hall response thus emerges from the interplay between Landau quantization and boundary-induced guiding-center discretization, which together determine the spectrum and occupation of chiral edge channels. These results establish boundary-induced quantization as the microscopic origin of quantum Hall transport and provide a unified description of both integer and fractional regimes within conventional quantum mechanics.

I. INTRODUCTION

The coexistence of integer and fractional quantum Hall plateaus in the same device remains one of the central unresolved microscopic questions in condensed-matter physics. Integer quantization is traditionally attributed to Landau levels of noninteracting electrons, whereas fractional plateaus are explained through strongly correlated many-body states. Although each framework successfully reproduces specific experimental features, their conceptual separation leaves open a fundamental issue: what physical mechanism in real, finite systems generates the universal hierarchy of Hall plateaus and connects bulk quantization to transport?

Since its discovery [1], the quantum Hall effect has become a paradigmatic example of macroscopic quantization [2–7]. Topological invariants, bulk–edge correspondence, and many-body approaches have clarified the robustness and universality of Hall transport. Yet these descriptions often rely on periodic geometries or treat edge states phenomenologically, leaving the microscopic role of confinement and boundary conditions largely implicit. Consequently, the mechanism by which finite boundaries shape the edge spectrum and produce the observed plateau hierarchy has remained incomplete. The present work does not seek to replace bulk topological or many-body descriptions of the quantum Hall effect; rather, it identifies the role of physically consistent boundary conditions in finite systems as a missing microscopic ingredient linking Landau quantization to the observed

plateau hierarchy.

In any physical realization of the quantum Hall effect, the two-dimensional electron system is spatially confined by geometry, electrostatics, and edge structure. Boundaries therefore constitute intrinsic constraints on the electronic wave functions. When a strong magnetic field drives carriers toward the sample edges, Landau states must satisfy boundary conditions that discretize the guiding-center coordinate and the longitudinal momentum of chiral modes. This boundary-induced quantization directly determines the multiplicity and structure of edge channels and therefore the transport spectrum. The absence of a microscopic treatment of this mechanism constitutes a missing bridge between Landau quantization and the hierarchy of Hall plateaus.

Here we show that boundary-induced quantization of edge states provides this bridge. Starting from the Landau problem in laterally confined geometries, we demonstrate that Dirichlet, Neumann, and mixed boundary conditions generate families of chiral edge modes with boundary-dependent multiplicities. Incorporated into an edge-transport description, these spectra reproduce the integer Hall sequence and yield a structured hierarchy of fractional filling factors within the same microscopic description.

We further show that a weak Hall-induced parity-breaking contribution reorganizes the low-energy edge spectrum while preserving the Landau-level ordering that governs the bulk states. The resulting energy shifts are localized near the boundaries, grow with guiding-center displacement, and scale inversely with the Landau index n ,

so their impact is strongest for the lowest levels at strong magnetic fields. In this regime the asymmetry selectively redistributes and pins additional chiral edge branches near the Fermi energy, enhancing the effective edge-state multiplicity and stabilizing the prominent fractional plateaus observed experimentally. Within this description, the integer and fractional quantum Hall effects emerge not as fundamentally distinct phenomena but as complementary manifestations of a single boundary-quantized edge structure shaped by confinement and controlled symmetry breaking.

The aim of this work is to establish a unified analytical description of edge-state quantization in laterally confined two-dimensional electron systems subjected to strong perpendicular magnetic fields. The analysis proceeds at two interconnected levels.

First, we determine how physically consistent boundary conditions imposed on Landau wave functions – Dirichlet, Neumann, and mixed (Robin-type) conditions – quantize both guiding-center positions and longitudinal edge momenta. Although these conditions differ in mathematical form and physical interpretation, they produce closely related edge localization and channel densities; their essential differences emerge in the allowed degeneracies and in the resulting filling-factor sequences.

Second, we introduce controlled symmetry breaking through a physically defined parameter associated with Hall-bias-induced edge asymmetry, incorporating structural imbalance, tunneling, and unequal edge transmission. This parameter is not phenomenological: its magnitude is determined by the boundary conditions and transport geometry rather than by fitting. It reorganizes the boundary-quantized edge spectrum while leaving the bulk cyclotron quantization as the underlying structure of the problem. The effect is essential for reproducing the high-field fractional hierarchy. By disentangling boundary-induced multiplicities from genuine parity-breaking effects, the analysis gains both conceptual transparency and predictive power.

In contrast to bulk topological formulations based on periodic boundary conditions or Chern invariants [2, 7], the present approach remains entirely within standard quantum mechanics and treats systems with explicit physical boundaries. The resulting boundary-quantized edge spectra feed directly into the Landauer–Büttiker transport formalism and lead to a closed analytical expression for the Hall resistance,

$$\rho_{xy} = \frac{h}{e^2 \nu_{\text{eff}}}, \quad \nu_{\text{eff}} = \frac{\nu_p}{\nu_c} \nu_n, \quad (1)$$

from which both integer and fractional Hall structures follow within a single microscopic description.

Figure 1 illustrates the central mechanism: boundary conditions discretize guiding centers near the sample edges and generate families of localized chiral states whose multiplicities depend on the boundary class. These spectra constitute the microscopic input for transport and deter-

mine the hierarchy of Hall plateaus.

The remainder of the paper develops this analysis by deriving the boundary-induced quantization of guiding centers and longitudinal momenta, introducing controlled parity breaking, and establishing the connection between edge spectra and macroscopic transport within the Landauer–Büttiker formalism, with direct comparison to experiment. The Appendices provide additional derivations and wave-function analyses supporting the main results.

II. BOUNDARY-INDUCED QUANTIZATION OF EDGE STATES

Quantization in confined quantum systems arises from the interplay between geometric confinement and admissibility conditions imposed on the wave function. The confining potential defines the spatial domain accessible to the particle, while the boundary conditions determine which wave functions are physically allowed within that domain. When an additional constraint restricts the spatial structure of admissible states, it becomes the origin of discrete spectra.

In the quantum Hall problem, confinement arises at two distinct and hierarchically ordered levels. The primary confinement is magnetic: the perpendicular field quantizes cyclotron motion and produces the Landau eigenstates, establishing the first level of quantization independently of any sample boundaries. Lateral confinement associated with the finite width of the device then acts on these pre-existing states. Its role is not to generate new transverse eigenmodes, but to define the accessible spatial domain and restrict the physically allowed positions of the Landau wave packets relative to the edges.

To make this distinction explicit, we represent the Hall bar as a stripe of width L_y through an auxiliary transverse potential

$$V(y) = \begin{cases} 0, & |y| < L_y/2, \\ V_0, & |y| \geq L_y/2, \end{cases} \quad (2)$$

with V_0 taken large compared to the Landau-level spacing. This potential is not intended as a microscopic model of edge electrostatics; it serves only to define the transverse limits $y = \pm L_y/2$ at which admissibility conditions must be imposed.

Within the effective-mass and independent-particle approximations, the Schrödinger equation in the Landau gauge $\mathbf{A} = -By\hat{x}$ reads

$$\left[\frac{1}{2m^*} (-i\hbar\nabla - e\mathbf{A})^2 + V(y) \right] \Psi(x, y) = E\Psi(x, y). \quad (3)$$

We first recall the solutions in the absence of lateral confinement. For $V(y) = 0$, the problem is separable, $\Psi(x, y) = e^{ik_x x} \eta(y)$, and Eq. (3) reduces to a

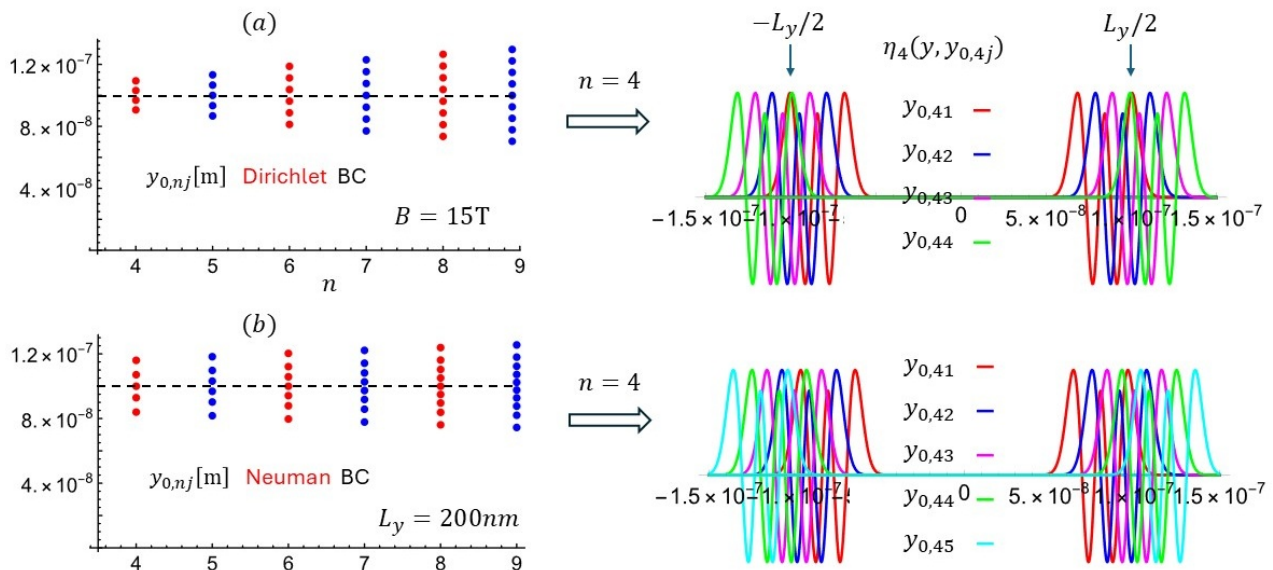


FIG. 1. Quantized guiding centers obtained from Dirichlet and Neumann boundary conditions, together with the corresponding Landau wave functions evaluated at those centers. Panels (a) and (b) show the guiding-center positions $y_{0,nj}$ obtained from Eqs. (8) and (9), respectively. In the right-hand column, the Landau functions for $n = 4$ are plotted at the guiding-center positions indicated in the left column. The boundary conditions place the guiding centers near the sample edges and produce similar edge localization. The Robin spectrum, shown in Fig. 9, consists of the Dirichlet spectrum supplemented by two additional guiding-center positions located near the inflection points of the Landau wave packet envelope. The magnetic field is $B = 15$ T and the stripe width is $L_y = 0.2 \mu\text{m}$.

one-dimensional harmonic oscillator centered at

$$y_0 = -k_x \ell_B^2, \quad (4)$$

where $\ell_B = \sqrt{\hbar/eB}$ is the magnetic length:

$$\left[-\frac{d^2}{dy^2} + \frac{1}{\ell_B^4} (y - y_0)^2 \right] \eta(y) = \frac{2m^*E}{\hbar^2} \eta(y). \quad (5)$$

The normalized eigenfunctions are the displaced Hermite–Gaussian Landau states

$$\eta_n(y) = C_n \exp\left[-\frac{(y - y_0)^2}{2\ell_B^2}\right] H_n\left(\frac{y - y_0}{\ell_B}\right), \quad (6)$$

with discrete energies

$$E_n = \hbar\omega_c \left(n + \frac{1}{2}\right), \quad \omega_c = \frac{eB}{m^*}. \quad (7)$$

These transverse states are determined entirely by magnetic quantization and exist independently of lateral confinement. They are not standing waves created by the confining potential, but localized Landau wave packets whose guiding-center coordinate y_0 can take any value in an extended system. Lateral finiteness therefore does not generate new transverse modes; it restricts the spatial locations available to these pre-existing states relative to the sample edges.

When the transverse states already possess a fixed internal structure, boundary conditions select the configurations compatible with the finite geometry and thereby act as an additional quantization mechanism.

The present problem belongs to this class. Landau eigenfunctions are Hermite–Gaussian packets characterized by a discrete set of nodes, extrema, and inflection points. Imposing boundary conditions therefore does not merely truncate the wave function; it determines which of these structural features can coincide with the edges and thus directly selects the allowed guiding-center positions and the associated longitudinal momenta.

In a stripe geometry, admissibility must be enforced at $y = \pm L_y/2$. Different boundary prescriptions select different geometric features of the Hermite–Gaussian envelope:

- Dirichlet conditions align the zeros of the Hermite polynomial with the boundaries.
- Neumann conditions pin the extrema of the wave packet at the edges.
- Robin conditions constrain its curvature and effectively select outer inflection structures.

Because these structural features occur with comparable spatial density, the resulting guiding-center locations are similar across boundary classes, while their multiplicities differ in a systematic and physically transparent

manner. The detailed shape of the confining potential therefore becomes secondary: its essential role is to define the transverse domain, whereas the boundary conditions determine the selected spectrum.

We now make these boundary constraints explicit. The transverse Landau wave functions must satisfy boundary conditions at $y = \pm L_y/2$ of the form

$$\text{Dirichlet:} \quad \eta_n|_{y=\pm L_y/2} = 0, \quad (8)$$

$$\text{Neumann:} \quad \left. \frac{d\eta_n}{dy} \right|_{y=\pm L_y/2} = 0, \quad (9)$$

$$\text{Robin:} \quad \left(\eta_n + \frac{d\eta_n}{dy} \right) \Big|_{y=\pm L_y/2} = 0. \quad (10)$$

For the unit-coefficient choice adopted here, the Robin condition is equivalent to a curvature constraint; a short derivation is provided in Appendix A. The Neumann and Robin conditions follow from the requirement that the probability current remain tangent to the boundary, so that its normal component vanishes at the edges,[9] whereas the Dirichlet condition is imposed directly as a boundary admissibility constraint.

Imposing any of these conditions at both edges restricts the allowed positions of the guiding center and therefore quantizes the longitudinal momentum k_x . The boundary does not generate new transverse modes; instead, it selects a discrete set of admissible Hermite–Gaussian wave packets localized near the edges. The resulting channel multiplicities depend on which structural feature of the wave packet is pinned at the boundaries and thus on the boundary class itself.

To implement this quantization explicitly, it is convenient to introduce the dimensionless variable

$$\xi = \frac{\pm L_y/2 - y_0}{\ell_B}. \quad (11)$$

The boundary condition determines the roots ξ_{nj} and thus yields a discrete spectrum of guiding centers for any effective width L_y . Using $k_x = -y_0/\ell_B^2$, the corresponding quantized longitudinal momenta are

$$k_{x,nj} = \frac{1}{\ell_B} \left(\xi_{nj} \pm \frac{L_y}{2\ell_B} \right). \quad (12)$$

As illustrated in Fig. 1, discretized guiding-center positions for $n = 4, 5, \dots, 9$ are shown together with the localized eigen-wave packets near the edge at $L_y/2$. The right column displays the transverse wave packets $\eta_{A_j}(y)$ for $n = 4$: the upper panel corresponds to Dirichlet boundary conditions with $j = 1, \dots, 4$, while the lower panel corresponds to Neumann boundary conditions with $j = 1, \dots, 5$. Panel (a) shows that Dirichlet boundary conditions yield n guiding centers for the n th Landau level, whereas panel (b) shows that Neumann boundary conditions increase this number to $n + 1$; the corresponding Robin spectrum, presented in Appendix B, contains $n + 2$

solutions. Although the resulting spectra are closely related for Dirichlet, Neumann, and Robin conditions, they exhibit systematic differences in edge-channel multiplicity.

These multiplicities translate directly into different effective channel weights in transport. When normalized to the current carried by a Dirichlet edge channel, a Neumann channel contributes a fraction $n/(n+1)$ of that current, while a Robin channel contributes $n/(n+2)$. These fractional factors arise purely from boundary-induced channel counting and anticipate the effective filling factors that emerge within the Landauer–Büttiker description. Their physical interpretation in terms of boundary-induced quantization and vanishing normal current is discussed in Appendix B.

The associated transverse magnetic confinement energy of each edge channel is

$$U_{nj} = \frac{\hbar\omega_c}{2} \xi_{nj}^2, \quad (13)$$

and the total energy can be written as $E_{nj} = K_{nj} + U_{nj}$, where $K_{nj} = \hbar^2 k_{x,nj}^2 / 2m^*$.

Importantly, this geometric quantization does not modify the Landau energy E_n in Eq. (7), but redistributes it between longitudinal kinetic and transverse magnetic confinement contributions within a given Landau level.

Only those edge channels whose total energy lies sufficiently close to the Fermi energy contribute to transport, establishing the microscopic link between boundary-induced quantization and quantized Hall conductance.

To visualize this redistribution and to make explicit the relation between the Landau index n and the discretized longitudinal momenta $k_{x,nj}$, we now introduce approximate expressions for the guiding-center eigenvalues ξ_{nj} obtained under the Robin boundary condition. These approximations provide analytical insight into the channel structure and are instrumental for the Landauer–Büttiker analysis that follows.

For both even and odd n , the approximate eigenvalues can be written as

$$\xi_{nj} \simeq \mp \sqrt{2n+1} \pm (j-1) \frac{\Delta y_{0,nj}}{\ell_B}, \quad j = 1, 2, \dots, n+2, \quad (14)$$

where the spacing between adjacent guiding centers is

$$\Delta y_{0,nj} \simeq \ell_B \frac{2\sqrt{2n+1}}{n+1}. \quad (15)$$

These expressions converge rapidly to the exact numerical roots for fixed j as n increases. The corresponding approximate longitudinal momenta for the Robin condition are

$$k_{x,nj} = -\frac{y_{0,nj}}{\ell_B^2} \simeq \pm \frac{\sqrt{2n+1}}{\ell_B} + \frac{(j-1)\Delta y_{0,nj}}{\ell_B^2} \mp \frac{L_y}{2\ell_B^2}, \quad (16)$$

yielding $n + 2$ discrete momentum values for each Landau level.

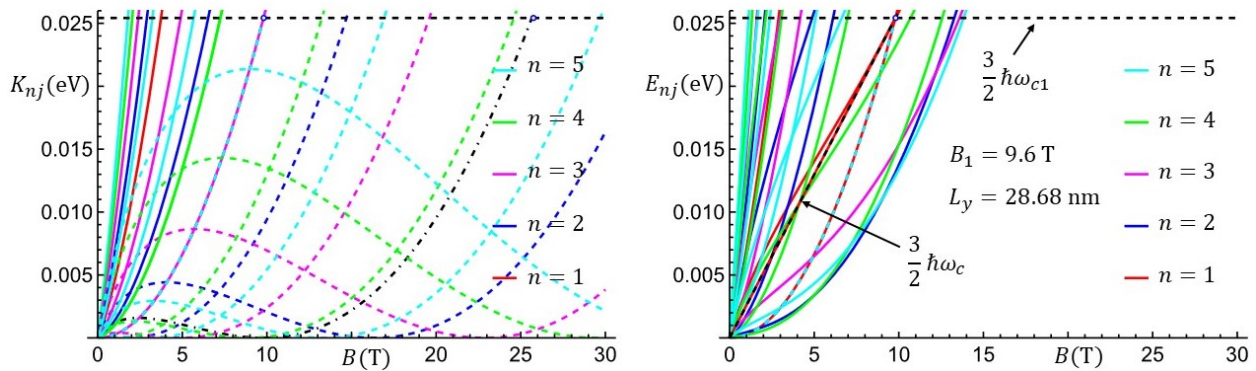


FIG. 2. Kinetic and total energies of edge channels as functions of magnetic field. Left panel: longitudinal kinetic energies $K_{nj} = \hbar^2 k_{x,nj}^2 / 2m^*$ for the first five Landau levels, computed from the exact quantized momenta in Eq. (12). Approximately half of the kinetic branches remain below the Fermi energy. Right panel: total energies $E_{nj} = K_{nj} + U_{nj}$. Including the magnetic confinement potential U_{nj} reorders the spectrum: branches associated with large $|\xi_{nj}|$ are shifted upward, while those with small or vanishing ξ_{nj} experience smaller energy shifts. As a result, fewer channels remain below E_F , whereas the $\xi_{nj} = 0$ branches remain purely kinetic and evolve together with the $n = 1$ Landau level. The persistence (pinning) of selected channels after the bulk Landau level crosses E_F constitutes a microscopic mechanism responsible for residual chiral edge channels and, consequently, for the emergence of fractional Hall plateaus. Parameters are indicated in the plots; details on the effective stripe width L_y are provided in the Supplementary Information.

These analytical expressions allow one to follow directly the evolution of edge channels with magnetic field. The interplay between the longitudinal kinetic energy K_{nj} and the transverse magnetic confinement energy U_{nj} determines which channels remain active in transport as the field increases. Details on the relation between momentum sign, edge localization, and channel exchange are provided in Appendix C.

Figure 2 compares the kinetic energies $K_{nj} = (\hbar^2 / 2m^*) k_{x,nj}^2$ with the corresponding total energies $E_{nj} = K_{nj} + U_{nj}$. While the kinetic spectrum alone exhibits multiple low-energy branches, the inclusion of U_{nj} selectively shifts channels with large $|\xi_{nj}|$ upward, leaving only those with small or vanishing $|\xi_{nj}|$ below the Fermi energy.

The $\xi_{nj} = 0$ modes, which occur for odd Landau indices, remain purely kinetic and evolve together with the $n = 1$ Landau level. These pinned chiral channels preserve current continuity even after the bulk Landau level crosses E_F . Thus, although magnetic confinement progressively reduces the number of conducting channels, it does not eliminate them completely. The surviving edge states provide the microscopic basis for the residual fractional Hall plateaus observed experimentally, as made explicit in the transport analysis that follows.

This correspondence between guiding-center quantization, energy redistribution, and channel survival establishes the microscopic foundation for the Hall resistance derived within the Landauer–Büttiker framework. While boundary conditions alone account for most observed Hall plateaus, the next section incorporates the effect of the Hall potential, which further refines the plateau structure.

III. EDGE SPECTRA FROM BOUNDARY CONDITIONS AND PARITY BREAKING

In the previous section we analyzed the consequences of boundary conditions alone on the quantization of guiding centers and the resulting multiplicity of edge states. Imposing Dirichlet, Neumann, or Robin boundary conditions on Landau wave functions in a laterally finite system produces families of edge states whose number scales with the Landau index, with small but systematic differences among the three cases. These boundary-induced multiplicities generate a rich hierarchy of edge channels, providing essential microscopic input required for the quantization of Hall transport.

We now extend this analysis by incorporating, in addition to boundary conditions, a controlled parity-breaking mechanism that reflects the fact that, under Hall bias, the two edges of the sample are not energetically equivalent, even though both remain sharply confined. In the quantum Hall regime, chiral edge states and the strong suppression of backscattering are essential ingredients in the emergence of quantized Hall resistance. Within the Landauer–Büttiker framework, transport is described in terms of edge channels propagating along the upper and lower boundaries, characterized by chemical potentials μ_A and μ_B . Their difference defines the Hall potential $V_H = (\mu_A - \mu_B) / e$.

In idealized treatments of open quantum Hall systems, the Hall potential is introduced at the level of electrochemical transport and does not explicitly enter the single-particle Schrödinger equation. Here we retain a small, controlled fraction of the associated transverse force in order to describe the microscopic asymmetry between the two edges. This residual contribution captures the

fact that, under Hall bias, the edges are not energetically equivalent even though both remain sharply confined.

Specifically, we introduce a weak linear term in the transverse potential, proportional to the coordinate y ,

$$V(y) = \begin{cases} b e B v_x y, & |y| < L_y/2, \\ V_0, & |y| \geq L_y/2, \end{cases} \quad (17)$$

where $0 < b \ll 1$ is a dimensionless parameter quantifying the fraction of the Hall force retained in the transverse dynamics. This term tilts the magnetic confinement potential and breaks the parity symmetry $y \rightarrow -y$ of the ideal Landau problem. Using $v_x = \hbar k_x / m^* = -y_0 \omega_c$, the parity-breaking contribution can be expressed entirely in terms of the guiding-center coordinate y_0 .

With this modification, the transverse Schrödinger equation becomes

$$\left[-\frac{d^2}{dy^2} + \frac{1}{\ell_B^4} (y - y_0)^2 + b \frac{y_0}{\ell_B^4} y \right] \eta(y) = \frac{2m^* E}{\hbar^2} \eta(y), \quad (18)$$

where $y_0 = -k_x \ell_B^2$ is the guiding-center coordinate. The equation remains exactly solvable and preserves the Landau-level indexing, while shifting the effective oscillator center and redistributing the energies of edge-localized modes within each Landau level.

The normalized solutions can be written in the compact form

$$\eta(y) = c_n \exp\left[-\frac{(y - (1+b)y_0)^2}{2\ell_B^2}\right] H_{n'}\left(\frac{y - (1+b)y_0}{\ell_B}\right), \quad (19)$$

where the effective polynomial index is

$$n'(n, b) = n + \frac{b(b+2)}{2n} \frac{L_y}{\ell_{B_1}}. \quad (20)$$

The quantity n' is not a new Landau quantum number but an effective index characterizing boundary-compatible solutions of the parity-broken problem. Integer values of n' identify the transverse wave packets that satisfy the boundary conditions and therefore correspond to physically realizable edge eigenstates. Here ℓ_{B_1} denotes the magnetic length evaluated at the magnetic field corresponding to the $n = 1$ Hall plateau. The corresponding energy eigenvalues are

$$E = \hbar \omega_c \left(n + \frac{1}{2} \right) - b(b+2) \frac{y_0^2}{\ell_B^2} \hbar \omega_c. \quad (21)$$

Several immediate consequences follow. The magnitude of the parity-breaking parameter required to reproduce the fractional sequences discussed below is small, so that the Landau-level ordering remains the organizing structure of the spectrum. The associated energy shift grows with guiding-center displacement (equivalently with $k_x^2 \ell_B^2$), localizing its impact near the sample boundaries and making it increasingly relevant at strong magnetic

fields. In addition, the shift scales inversely with the Landau index n , so that its spectral effect is strongest for the lowest levels. As a result, parity breaking does not generate new edge modes but selectively stabilizes additional low-energy branches already permitted by boundary quantization, thereby enhancing the effective edge-state multiplicity.

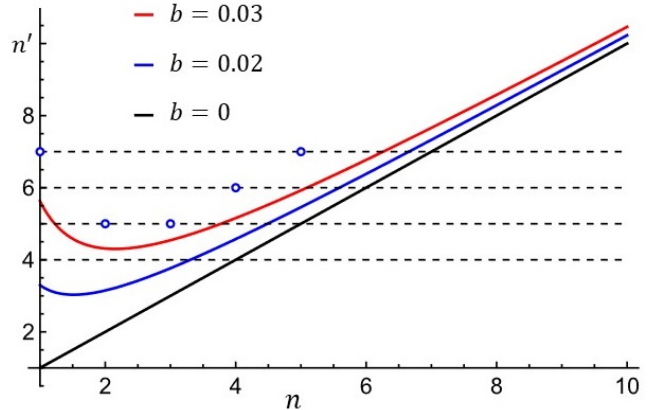


FIG. 3. Effective eigenfunction index n' and corresponding number of edge states, obtained under the Neumann boundary condition, as functions of the Landau index n and the parity-breaking parameter b . The solid curves show the analytical expression of $n'(n, b)$ in (20). Horizontal dashed lines indicate integer values of n' . Small circles denote the number of zeros of the Neumann boundary condition, $d\eta/dy|_{y=\pm L_y/2} = 0$, which correspond to local extrema of the Hermite–Gaussian envelope where the guiding centers are pinned by the boundary. For finite parity breaking (e.g. $b \simeq 0.03$), the resulting integer sequences exhibit a non-monotonic dependence on n , signaling an enhancement of low-energy edge-state multiplicity at small Landau indices.

A convenient way to quantify this effect is through the effective Hamiltonian order n' , whose integer part determines the number of available low-energy edge states for a given Landau index and parity-breaking strength. Equation (20) shows explicitly that parity breaking enhances the number of edge channels most strongly for $n = 1$ and $n = 2$, and that this enhancement depends nontrivially on b .

This behavior is illustrated in Fig. 3, which shows $n'(n, b)$ as a function of the Landau index for representative values of b . For intermediate parity breaking, $n'(n, b)$ exhibits a non-monotonic dependence on n . The intersections with integer values of n' , indicated by discrete points, correspond to the actual number of edge branches contributing at the transport energy scale. These sequences anticipate the channel multiplicities that enter the effective filling factors and the fractional Hall plateaus derived below.

At this stage, the role of parity breaking is purely microscopic. It reorganizes the edge spectrum by stabilizing additional long-lived low-energy branches without modi-

fying the bulk Landau quantization. Figure 3 shows, for example, the sequence (7, 5, 5, 6, 7, ...) of zeros of the Neumann boundary condition, corresponding to local extrema of the Landau wave function at the edge. Through the effective filling factor ν_{eff} , this sequence generates nearly the complete set of prominent fractional Hall plateaus observed experimentally in high-mobility samples.

Within this framework, the fractional quantum Hall effect emerges as the cumulative consequence of two single-particle mechanisms: (i) boundary-induced discretization of guiding centers and longitudinal momenta, and (ii) weak parity breaking that selectively enhances low-energy edge-state multiplicities. In the next section, these modified edge spectra are translated directly into quantized Hall resistance plateaus within the Landauer–Büttiker transport formalism.

IV. EDGE CHANNEL TRANSPORT AND HALL QUANTIZATION

Having established that physically consistent boundary conditions and controlled parity breaking generate a discrete hierarchy of chiral edge channels, we now examine how this microscopic edge structure translates into measurable transport.

Before introducing a specific transport formalism, it is essential to clarify how the counting, occupation, and energetic ordering of boundary-quantized edge states evolve as the magnetic field and Fermi energy are varied. In a finite Hall geometry, electrical conduction is mediated by boundary-confined states whose quantized longitudinal momenta determine both the number of available channels and their energetic alignment with the Fermi level.

IV.1. Boundary- and Symmetry-Induced Filling-Factor Hierarchies

At this stage the focus is not yet on transport coefficients but on the microscopic organization of the edge spectrum itself. The relevant quantity is the edge filling configuration, which reflects the partial occupation of boundary-quantized chiral channels associated with successive Landau levels and their edge-mode families. Boundary conditions fix the allowed guiding-center positions and therefore the channel multiplicities, while parity breaking selectively lifts degeneracies at low Landau indices. Together, these mechanisms generate a structured hierarchy of edge configurations that anticipates both integer and fractional Hall plateaus.

Substituting the quantized longitudinal momenta into the total energy expression yields the discrete edge-state energies

$$E_{nj} = \frac{\hbar^2}{2m^*} \frac{1}{\ell_B^2} \left(\xi_{nj} \pm \frac{L_y}{2\ell_B} \right)^2 + \frac{\hbar\omega_c}{2} \xi_{nj}^2. \quad (22)$$

For the present discussion, the explicit analytical form of E_{nj} is less important than its ordering and spacing. The discrete set of energies defines the hierarchy of edge channels associated with each Landau level and determines which of them lie closest to the Fermi energy as the magnetic field varies.

The separation between neighboring edge branches introduces a characteristic energy scale, typically of order $\hbar\omega_c/\sqrt{n+1}$, which governs the progressive activation and depopulation of channels. Low-energy branches remain pinned near the Fermi level over finite magnetic-field intervals, while higher branches shift away more rapidly. This energetic hierarchy provides the microscopic basis for the emergence of plateau structures.

We first distinguish the number of bulk Landau-level families that are energetically available to supply edge states. This quantity,

$$\nu_n \equiv n_{\text{max}},$$

counts the highest Landau index intersecting the Fermi energy and represents the reservoir of edge-mode families generated by magnetic quantization. It is a bulk spectral quantity and does not coincide with the experimentally measured Hall filling factor.

Boundary conditions then determine how many edge channels are realized from each Landau family. The total number of available chiral channels is therefore

$$\nu_c = \begin{cases} n_{\text{max}}, & \text{Dirichlet boundary condition,} \\ n_{\text{max}} + 1, & \text{Neumann boundary condition,} \\ n_{\text{max}} + 2, & \text{Robin boundary condition.} \end{cases}$$

Parity breaking further redistributes the energies of these channels and enhances their multiplicity at small Landau indices, without modifying the underlying Landau-level structure. The combined action of boundary constraints and symmetry breaking therefore produces a discrete hierarchy of admissible edge-state configurations.

Within this hierarchy, the experimentally relevant filling factors arise from the energetic alignment of boundary-quantized channels with the Fermi level. The ordering and spacing of the edge-state energies determine which channels remain active as the magnetic field varies.

An immediate consequence is that the spacing between effective filling configurations is not imposed phenomenologically but follows from the density of boundary-allowed channel configurations. Plateau widths therefore follow directly from the discrete structure of the guiding-center spectrum and its multiplicities: densely spaced configurations produce narrow plateaus, while sparser regions generate broader ones.

This boundary- and symmetry-induced hierarchy provides the microscopic input required for transport. The translation from channel occupation to measurable conductance is carried out within the Landauer–Büttiker framework, which we now introduce.

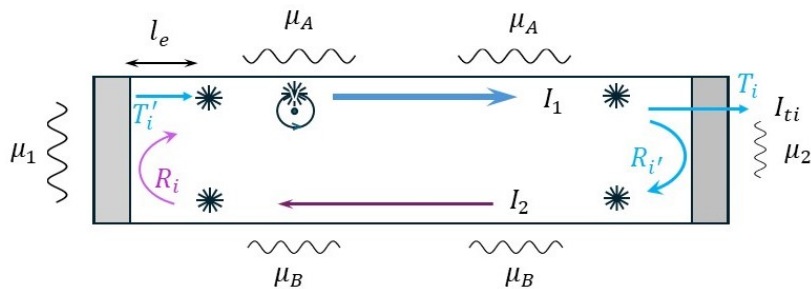


FIG. 4. Schematic representation of the Landauer–Büttiker transport picture applied to the parity-quantized Landau spectrum. Electrons are injected from the left reservoir (chemical potential μ_1) into the quantized edge channels whose total energies E_{nj} match the Fermi level E_F ; resonant tunneling across the contact barrier selectively populates these discrete states, while electrons injected into non-resonant states relax inelastically toward them. Inside the sample, edge electrons propagate chirally along equipotential contours with constant longitudinal momentum $k_{x,nj}$ and strongly suppressed backscattering. At the drain contact (chemical potential μ_2), part of the incoming flux is transmitted into the reservoir (forming the transmitted current I_t) and part is reflected back into lower edge channels, contributing to the reflected edge flux. The transmission coefficient T_j for individual channel j results from the sum over reservoir feeding states, and the net transmission summed over the ν_p populated channels equals the T_{1p} used in the text (see Eqs. 23–25), providing the flux-conservation link between microscopic channel transmissions and the macroscopic currents.

IV.2. Landauer–Büttiker formulation with parity-dependent edge channels

Before introducing the explicit Landauer–Büttiker transport relations, it is useful to clarify the physical mechanism by which boundary-quantized edge states become populated and contribute to current flow.

In the Landauer–Büttiker picture, electrons in the source reservoir occupy an almost continuous distribution of states around the Fermi energy E_F , thermally broadened by $\sim k_B T$. When the total energy of an edge state, $E_{nj} = K_{nj} + U_{nj}$, aligns with E_F , electrons within this thermal window can tunnel across the contact barrier and, after inelastic relaxation, populate the quantized edge state j with an effective probability $T'_j = \sum_{i=1}^M T'_{ji}$ determined by the contact transmission matrix elements rather than by bulk occupation statistics.

Because the edge states belonging to a given Landau level have slightly different energies, their population evolves systematically as the magnetic field varies. Lower-energy branches become occupied later and remain localized near the Fermi level, while higher-energy branches depopulate and shift upward in energy. Once populated, these edge channels behave as effectively one-dimensional, phase-coherent chiral conduits linking source and drain.

Electrons propagate along equipotential contours with nearly constant longitudinal momentum $k_{x,nj}$ and strongly suppressed backscattering. At the drain contact (μ_2), a fraction of the incident flux is transmitted into the reservoir, contributing to the total current I_t , while the remainder is reflected into lower-energy edge channels along the opposite boundary. This partial transmission and reflection process is quantitatively described by the contact transmission and reflection coefficients.

The natural current scale in this regime is set by the

number of bulk Landau-level families available to supply edge conduction. Using the Landau-index filling introduced above, $\nu_n = n_{\max}$, we identify the number of occupied Landau levels capable of feeding edge-mode families.

Each such Landau family provides, under ideal injection, the capacity to carry one quantum of conductance. In the phase-coherent limit, the ideal edge current I^{ed} injected along the upper boundary at chemical potential μ_A , referenced to μ_2 , is therefore

$$I^{\text{ed}} = \frac{e}{h} \nu_n (\mu_A - \mu_2).$$

This quantity represents the intrinsic injection scale set by magnetic quantization; the measurable transmitted current is subsequently determined by the boundary-resolved channel multiplicities and the corresponding transmission and reflection processes at the contacts.

Once the boundary-quantized edge channels and their energetic ordering are established, their contribution to electrical transport can be treated in a direct and unambiguous manner within the Landauer–Büttiker formalism. This framework is particularly appropriate here because current is carried by chiral edge modes whose number, multiplicity, and alignment with the Fermi level are fixed microscopically by boundary conditions and controlled parity breaking.

Unlike bulk linear-response approaches, the Landauer–Büttiker picture connects discrete edge spectra to measurable currents through transmission and reflection processes at the contacts, without requiring disorder-induced localization or spatial averaging.

Following Ref. 8, the transmission and reflection coefficients between the reservoirs and the populated edge channels at contact 1 are

$$T_{1p} = \sum_{j=1}^M \sum_{i=1}^{\nu_p} T_{ji}, \quad R_{1p} = \sum_{i=1}^{\nu_p} \sum_{l=1}^{\nu_p} R_{i'l}, \quad (23)$$

where ν_p denotes the number of edge channels populated at the Fermi level. Similarly, at contact 2,

$$T_{2p} = \sum_{j=1}^{M'} \sum_{l=1}^{\nu_p} T_{jl}, \quad R_{2p} = \sum_{l=1}^{\nu_p} \sum_{l'=1}^{\nu_p} R_{l'l}. \quad (24)$$

Flux conservation requires

$$T_{1p} + R_{1p} = \nu_p, \quad T_{2p} + R_{2p} = \nu_p. \quad (25)$$

Within the Landauer description, the current injected from a reservoir at chemical potential μ into the j th populated edge channel is

$$I_j = \frac{e}{h} (\mu - \mu_0) T_j, \quad (26)$$

where T_j is the transmission probability into that channel and $\partial n_e / \partial E_j = 1/hv_j$ has been used for the one-dimensional density of states.

The total current leaving contact 1 contains both the injected component and the portion reflected from the opposite boundary,

$$I_{1p} = \frac{e}{h} T_{1p} (\mu_1 - \mu_2) + I_{2R}^{\text{ed}}. \quad (27)$$

The edge current carried by the populated channels can be expressed in terms of the ideal edge-current scale I^{ed} introduced above. Because only a subset ν_p of the ν_c boundary-allowed channels is energetically aligned with the Fermi level, the injected edge current is reduced by the ratio ν_p/ν_c . One obtains

$$I_{1p}^{\text{ed}} = \frac{\nu_p}{\nu_c} I^{\text{ed}} = \frac{e}{h} \frac{\nu_p}{\nu_c} \nu_n (\mu_A - \mu_2), \quad (28)$$

To simplify the notation and to isolate the physically relevant combination of microscopic ingredients, we introduce the effective filling factor

$$\nu_{\text{eff}} = \frac{\nu_p}{\nu_c} \nu_n, \quad (29)$$

which combines three distinct contributions: the bulk Landau-level supply (ν_n), the boundary-induced channel multiplicity (ν_c), and the number of channels actually populated near the Fermi level (ν_p).

Using the flux-conservation relations (25), Eq. (28) can be rewritten as

$$\begin{aligned} I_{1p}^{\text{ed}} &= \frac{e}{h} \frac{\nu_{\text{eff}}}{\nu_p} (T_{2p} + R_{2p}) (\mu_A - \mu_2) \\ &= I_{1t} + I_{1R}, \end{aligned} \quad (30)$$

with transmitted and reflected contributions

$$I_{1t} = \frac{e}{h} \frac{\nu_{\text{eff}}}{\nu_p} T_{2p} (\mu_A - \mu_2), \quad (31)$$

and

$$I_{1R} = \frac{e}{h} \frac{\nu_{\text{eff}}}{\nu_p} R_{2p} (\mu_A - \mu_2). \quad (32)$$

At contact 2, the edge current reads

$$\begin{aligned} I_{2p}^{\text{ed}} &= \frac{e}{h} \nu_{\text{eff}} (\mu_B - \mu_2) \\ &= \frac{e}{h} \frac{\nu_{\text{eff}}}{\nu_p} (T_{1p} + R_{1p}) (\mu_B - \mu_2). \end{aligned} \quad (33)$$

Combining these relations yields

$$T_{1p} (\mu_1 - \mu_2) + \frac{\nu_{\text{eff}}}{\nu_p} R_{1p} (\mu_B - \mu_2) = \nu_{\text{eff}} (\mu_A - \mu_2), \quad (34)$$

and

$$(\mu_B - \mu_2) = \frac{R_{2p}}{\nu_p} (\mu_A - \mu_2). \quad (35)$$

From these expressions,

$$\mu_A - \mu_2 = \frac{\nu_p^2}{\nu_{\text{eff}} \nu_p^2 - R_{1p} R_{2p}} T_{1p} (\mu_1 - \mu_2), \quad (36)$$

and

$$\mu_B - \mu_2 = \frac{\nu_p}{\nu_{\text{eff}} \nu_p^2 - R_{1p} R_{2p}} T_{1p} R_{2p} (\mu_1 - \mu_2). \quad (37)$$

IV.3. The Quantum Hall Resistance

With the microscopic edge spectrum fixed by boundary conditions and parity breaking, the Hall resistance follows directly from the imbalance of chemical potentials established between counterpropagating edge channels.

From Eqs. (36) and (37) we obtain

$$\mu_A - \mu_B = \frac{1}{\nu_{\text{eff}}} \frac{T_{1p} \nu_p (\nu_p - R_{2p})}{\nu_p^2 - R_{1p} R_{2p}} (\mu_1 - \mu_2), \quad (38)$$

and the transmitted current

$$I = \frac{e}{h} \frac{\nu_p T_{1p} T_{2p}}{\nu_p^2 - R_{1p} R_{2p}} (\mu_1 - \mu_2). \quad (39)$$

The Hall voltage $V_H = (\mu_A - \mu_B)/e$ and the current I therefore satisfy

$$V_H = \frac{1}{e \nu_{\text{eff}}} \frac{T_{1p} \nu_p T_{2p}}{\nu_p^2 - R_{1p} R_{2p}} (\mu_1 - \mu_2), \quad (40)$$

and

$$I = \frac{e}{\hbar} \frac{\nu_p T_{1p} T_{2p}}{\nu_p^2 - R_{1p} R_{2p}} (\mu_1 - \mu_2). \quad (41)$$

Eliminating the contact-dependent transmission and reflection coefficients from Eqs. (40) and (41) yields the universal relation

$$V_H = \frac{h}{e^2} \frac{I}{\nu_{\text{eff}}}, \quad (42)$$

which is independent of microscopic contact details and depends only on the effective filling factor defined by the boundary-quantized edge spectrum. The Hall resistivity therefore takes the compact form

$$\rho_{xy} = \frac{h}{e^2} \frac{\nu_c}{\nu_p \nu_n}. \quad (43)$$

This result expresses the quantized Hall resistance directly in terms of the microscopic hierarchy established earlier. Three integers determine the quantization pattern: the number of Landau-level families supplying edge modes (ν_n), the number of boundary-allowed channels set by confinement (ν_c), and the number of channels effectively populated near the Fermi level (ν_p). All three follow from magnetic quantization, boundary constraints, and controlled parity breaking, without introducing phenomenological transport parameters.

Because ν_c and ν_p arise from boundary-induced multiplicities and parity-controlled channel selection, their ratios naturally generate both integer and fractional values of ν_{eff} within the same microscopic framework.

This completes the microscopic-to-transport connection: boundary conditions alone determine the admissible edge-channel multiplicities and yield a first-principles prediction of the Hall resistance, while controlled parity breaking refines the spectrum and produces the corrected effective filling factor ν_{eff} , which, as shown in the next section, quantitatively reproduces the observed plateau hierarchy.

V. INTEGER AND FRACTIONAL HALL PLATEAUS FROM BOUNDARY-QUANTIZED EDGE TRANSPORT

We now determine explicitly the filling-factor sequences generated by each class of boundary condition.

Dirichlet boundary condition. For systems whose edge properties correspond to Dirichlet boundary conditions, the number of available edge channels fixed by the boundary coincides with the number of occupied Landau-level families,

$$\nu_c = \nu_n \equiv n_{\text{max}}.$$

The Hall resistivity therefore reduces to

$$\rho_{xy} = \frac{h}{e^2} \frac{1}{\nu_p}, \quad \nu_p = 1, 2, \dots, n_{\text{max}}, \quad (44)$$

which reproduces the standard integer quantum Hall effect (IQHE) sequence. This case therefore serves as the natural reference limit in which boundary quantization reproduces the conventional integer quantum Hall response.

We now examine how Neumann and Robin boundary conditions modify the edge spectrum. In contrast to the Dirichlet case, the boundary-induced change in edge-channel multiplicity generates additional admissible filling factors and leads naturally to the fractional plateaus observed experimentally.

Neumann boundary condition. For systems described by Neumann boundary conditions, the number of available edge channels is increased by one,

$$\nu_c = \nu_n + 1.$$

The effective filling factor then becomes

$$\nu_{\text{eff}} = \frac{\nu_p n_{\text{max}}}{n_{\text{max}} + 1}, \quad \nu_p = 1, 2, \dots, n_{\text{max}} + 1,$$

reflecting the presence of an additional boundary-allowed edge channel that can remain partially populated near the Fermi level. This construction generates a hierarchy of effective filling-factor sequences for all values of n_{max} . For clarity, we list here the lowest-order cases explicitly:

$$\begin{aligned} n_{\text{max}} = 1 &\Rightarrow \nu_{\text{eff}} = \frac{\nu_p}{2} = \left\{ \frac{1}{2}, 1 \right\}, \\ n_{\text{max}} = 2 &\Rightarrow \nu_{\text{eff}} = \frac{2\nu_p}{3} = \left\{ \frac{2}{3}, \frac{4}{3}, 2 \right\}, \\ n_{\text{max}} = 3 &\Rightarrow \nu_{\text{eff}} = \frac{3\nu_p}{4} = \left\{ \frac{3}{4}, \frac{3}{2}, \frac{9}{4}, 3 \right\}, \\ n_{\text{max}} = 4 &\Rightarrow \nu_{\text{eff}} = \frac{4\nu_p}{5} = \left\{ \frac{4}{5}, \frac{8}{5}, \dots, 4 \right\}. \end{aligned} \quad (45)$$

Higher values of n_{max} extend this sequence systematically, generating additional admissible fractions according to the same boundary-quantization rule.

Robin boundary condition. For systems whose edges are described by Robin boundary conditions, the number of available edge channels is increased by two,

$$\nu_c = \nu_n + 2.$$

The effective filling factor is now

$$\nu_{\text{eff}} = \frac{\nu_p n_{\text{max}}}{n_{\text{max}} + 2}, \quad \nu_p = 1, 2, \dots, n_{\text{max}} + 2,$$

corresponding to the presence of two additional boundary-allowed edge channels, one at each edge, whose occupation is controlled by the same energetic pinning mechanism. This construction generates a hierarchy of effective filling-factor sequences for all values of n_{max} under Robin

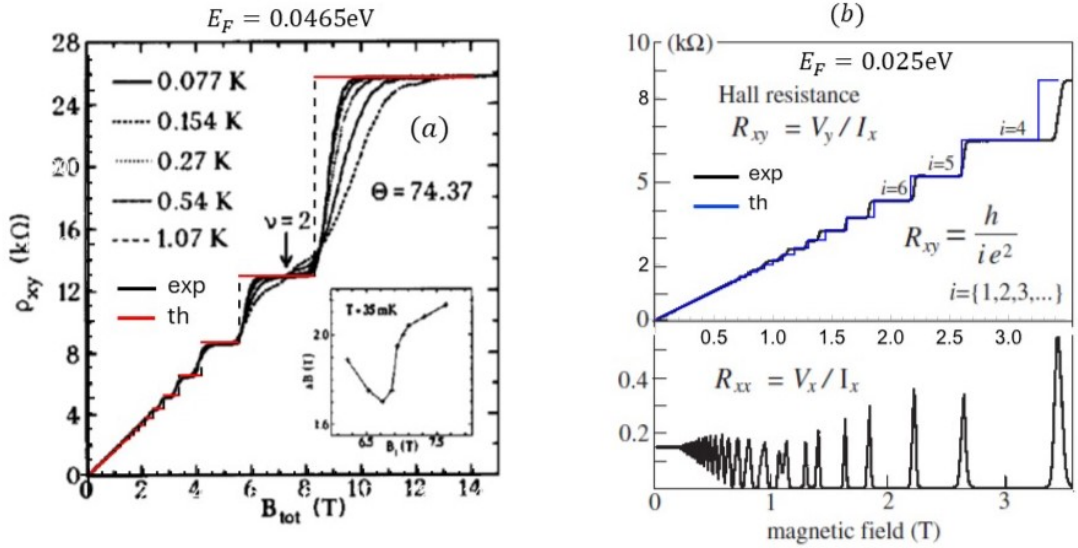


FIG. 5. Experimental and theoretical Hall resistance (in units of h/e^2). (a) Theoretical prediction compared with the experimental Hall-resistance curve measured in a two-dimensional electron system at a GaInAs/InP interface, reported in Ref. [10] (reproduced with permission from Elsevier). (b) Comparison between theory and experiment for a two-dimensional electron system in a GaAs/(AlGa)As heterostructure, reported in Ref. [11] (reproduced with permission from The Royal Society, UK). Theoretical curves were obtained from Eq. (48) using the boundary-determined effective filling factor for the Fermi energies indicated in each panel, without additional fitting parameters. Both integer and fractional plateaus arise from the same boundary-quantized edge spectrum.

boundary conditions. For clarity, we list here several representative low-order cases:

$$\begin{aligned}
 n_{\max} = 1 &\Rightarrow \nu_{\text{eff}} = \frac{\nu_p}{3} = \left\{ \frac{1}{3}, \frac{2}{3}, 1 \right\}, \\
 n_{\max} = 2 &\Rightarrow \nu_{\text{eff}} = \frac{2\nu_p}{4} = \left\{ \frac{1}{2}, 1, \frac{3}{2}, 2 \right\}, \\
 n_{\max} = 3 &\Rightarrow \nu_{\text{eff}} = \frac{3\nu_p}{5} = \left\{ \frac{3}{5}, \frac{6}{5}, \dots, 3 \right\}, \\
 n_{\max} = 4 &\Rightarrow \nu_{\text{eff}} = \frac{4\nu_p}{6} = \left\{ \frac{2}{3}, \frac{4}{3}, 2, \dots, 4 \right\}, \\
 n_{\max} = 5 &\Rightarrow \nu_{\text{eff}} = \frac{5\nu_p}{7} = \left\{ \frac{5}{7}, \frac{10}{7}, \dots, 5 \right\}.
 \end{aligned} \tag{46}$$

Higher values of n_{\max} extend this hierarchy systematically, producing additional admissible fractions according to the same boundary-quantization rule. In particular, the characteristic fractional values

$$\nu_{\text{eff}} = \frac{1}{3}, \frac{2}{3}, \frac{3}{5}, \frac{4}{5}, \frac{5}{7}, \dots$$

emerge naturally from the same finite-system quantization rules, without requiring electron-electron correlations, composite fermions, or disorder-induced localization as primary ingredients of the quantization mechanism.

This does not exclude the presence or importance of interactions and disorder in real samples; rather, it shows that the observed filling-factor hierarchy can already be generated at the level of boundary-controlled edge spectra,

with additional many-body and scattering effects acting on a structure that is intrinsically established by the boundary quantization.

Within this unified framework, the integer and fractional quantum Hall effects emerge as complementary manifestations of a common microscopic organizing mechanism: the discrete, boundary-dependent spectrum of edge states imposed by lateral confinement in a finite two-dimensional electron system.

Integer and fractional plateaus from boundary quantization To connect the boundary-controlled hierarchy with experimental observations, we now relate the effective filling-factor sequences to the magnetic-field dependence of the Hall resistance. Dirichlet boundary conditions reproduce the conventional integer sequence, while Neumann and Robin boundary conditions generate fractional structures through their modified edge-channel multiplicities.

A key ingredient in this comparison is the relation between the highest occupied Landau-level index and the total energy E_T ,

$$\nu_n = n_{\max} = \left\lfloor \frac{E_T - \hbar\omega_c/2}{\hbar\omega_c} \right\rfloor, \tag{47}$$

where $\lfloor x \rfloor$ denotes the integer part of x . In contrast to conventional Landau-level counting, this expression explicitly incorporates the zero-point contribution.

Microscopically, E_T corresponds to the discrete set of edge-state energies $E_{n_j} = K_{n_j} + U_{n_j}$ introduced above. It

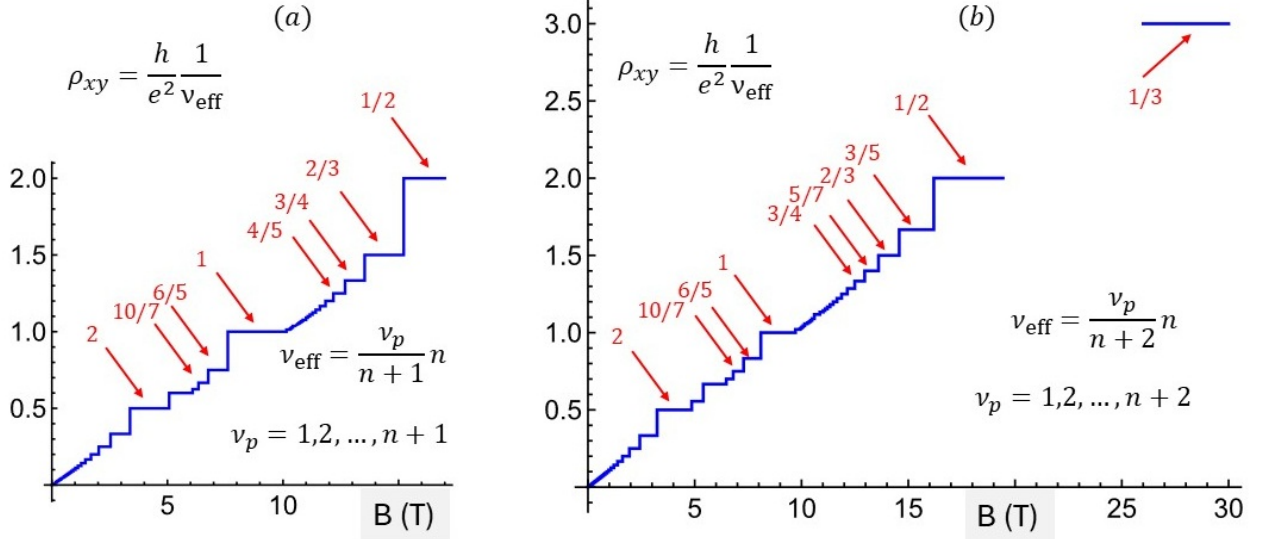


FIG. 6. Predicted Hall resistance $\rho_{xy} = (h/e^2)/\nu_{\text{eff}}$ obtained from boundary-quantized edge transport for (a) Neumann and (b) Robin boundary conditions as a function of magnetic field. The effective filling factors follow the sequences $\nu_{\text{eff}} = \nu_p/(n+1)$ for Neumann and $\nu_{\text{eff}} = \nu_p/(n+2)$ for Robin boundaries, with $\nu_p = 1, 2, \dots, n+1$ and $\nu_p = 1, 2, \dots, n+2$, respectively. The principal fractional plateaus are indicated in red. Plateau widths arise directly from the density of allowed filling factors generated by the boundary quantization. For the same magnetic-field interval, the Neumann hierarchy produces slightly broader plateaus, while the Robin case yields a denser but more closely spaced sequence extending toward smaller fractional values.

includes the Fermi energy E_F of the transmitted electrons, fixed by the reservoir chemical potentials, together with the Landau zero-point energy $\hbar\omega_c/2$. The inclusion of this contribution is essential for reproducing the correct low-field behavior of the Hall resistance. Neglecting this zero-point contribution leads to an incorrect low-field curvature of $\rho_{xy}(B)$, replacing the experimentally observed quasi-linear onset by a parabolic dependence. Accordingly, one may write $E_T \simeq E_F + \hbar\omega_c/2$, so that ν_n counts the number of fully occupied Landau levels lying below E_T , changing stepwise as the magnetic field varies.

Substituting Eq. (47) into the general expression for the Hall resistivity gives

$$\rho_{xy} = \frac{h}{e^2} \frac{1}{\frac{\nu_p}{\nu_c} \left[\frac{2\pi m^* E_F}{\hbar e B} \right]}, \quad (48)$$

where m^* is the effective electron mass. This relation does not introduce a new quantization rule; it connects the boundary-determined hierarchy of edge states with the magnetic-field-dependent indexing that governs transport measurements. In the Dirichlet limit, $\nu_c = n_{\text{max}}$ and therefore $\nu_{\text{eff}} = \nu_p$. In this case Eq. (48) should not be interpreted as a direct translation into bulk Landau degeneracy. Instead, it encodes the discrete set of transmitting edge states available up to the cutoff n_{max} , i.e., all branches with $n \leq n_{\text{max}}$. The experimentally observed plateau sequence then emerges as the magnetic field sequentially reveals this hierarchy when individual edge branches intersect the Fermi level and depopulate. Quantization therefore originates at the boundary level,

while the Landau-level description emerges as an effective macroscopic representation. The resulting magnetic-field dependence reproduces the quasi-linear sequence of Hall plateaus observed experimentally (Fig. 5) and clarifies the distinction between the discrete edge-state energies E_{nj} and the macroscopic Fermi energy E_F set by the reservoirs.

In Fig. 5(a,b) we compare the predicted Hall resistance with experimental results for integer plateaus in GaInAs/InP [10] and GaAs/(AlGa)As [11], using the corresponding effective masses and Fermi energies indicated in the figure. The theoretical curves, obtained assuming Dirichlet boundary conditions, are overlaid on the experimental data and show excellent agreement across the full magnetic-field range.

It is well established that, as the magnetic field increases and the cyclotron energy $\hbar\omega_c$ grows, the bulk Landau levels successively cross the Fermi energy. Within the present finite-system framework, however, a subset of low-energy edge branches can remain below the Fermi level even after the corresponding bulk Landau level has depopulated, as illustrated in Fig. 2. Fractional quantization therefore arises from the systematic survival of edge states that maintain current continuity across Landau-level transitions, without requiring electron-electron correlations as a primary quantization mechanism.

Figure 6 shows the Hall-resistance staircase predicted when the edge spectrum is determined solely by boundary conditions. In both panels the plateau structure is not imposed phenomenologically but emerges from the discrete hierarchy of effective filling factors allowed by

boundary-quantized edge channels.

In the Neumann case [Fig. 6(a)], the additional boundary-allowed channel increases the multiplicity of edge states, producing fractional plateaus such as $2/3$, $3/4$, $4/5$, and $6/5$. Because the admissible fractions are more sparsely distributed, the magnetic-field intervals over which ρ_{xy} remains constant are comparatively broad.

For Robin boundary conditions [Fig. 6(b)], two additional boundary-controlled channels generate a richer hierarchy that extends to smaller fractions, including $1/3$, $3/5$, and $5/7$. The higher density of admissible filling factors leads to a finer staircase and correspondingly narrower plateaus within the same field range.

Plateau widths therefore follow directly from the arithmetic structure of the boundary-generated filling-factor sequences. Above $\nu = 1$, the admissible fractions accumulate toward unity as $(n+1)/n$ and $(n+2)/n$ for Neumann and Robin boundaries, respectively, producing closely spaced steps. Below $\nu = 1$, the density of allowed fractions is comparatively lower and the plateaus become more widely separated. This intrinsic asymmetry in the distribution of admissible filling factors determines the characteristic widths of the Hall plateaus within the boundary-quantized spectrum.

Disorder and inelastic processes do not create these plateaus; rather, they broaden and round the staircase already established by the boundary quantization and by the arithmetic organization of the effective filling-factor hierarchy.

Boundary conditions discretize both the guiding-center positions y_0 and the longitudinal momenta of edge states. Within this framework, the Neumann condition may be viewed as a limiting case of the more general Robin boundary condition. More broadly, boundary confinement introduces a fine structure in the longitudinal edge momentum, analogous to a hyperfine splitting, whose magnitude sets the characteristic energy scale of fractional quantization.

We have shown that boundary conditions discretize both the guiding-center positions y_0 and the longitudinal momenta of edge states. More generally, this framework demonstrates that lateral confinement introduces a fine structure in the longitudinal edge momentum, analogous to a hyperfine splitting, whose magnitude sets the characteristic energy scale of fractional quantization.

Within this boundary-controlled picture, the integer hierarchy and a first set of fractional plateaus arise directly from the discrete spectrum of edge states. However, experiments at higher magnetic fields reveal additional fractional structures that cannot be accounted for by boundary quantization alone. To describe these regimes, we now include the parity-breaking mechanism introduced at the end of the previous section.

Fractional plateaus from parity-enhanced multiplicity
Retaining a small fraction of the Hall voltage as a parity-breaking perturbation increases the number of low-energy edge states, particularly at small Landau indices. When combined with a Neumann and Robin boundary condition, this perturbation further enhances the multiplicity

of boundary-supported channels, producing extended families of effective filling factors and enabling the emergence of additional high-field fractional plateaus.

To illustrate the robustness of this mechanism, we list two representative multiplicity patterns corresponding to nearby regions of the (b, L_y) parameter space. Both generate closely related fractional hierarchies and reproduce the principal experimentally observed plateaus.

TABLE I. Effective filling-factor sequences generated by parity-enhanced edge multiplicities for the representative sequence $(7, 5, 6, 7, 8, \dots)$.

n	ν_c	ν_n	Effective filling factors $\nu_{\text{eff}} = (\nu_p/\nu_c)\nu_n$
1	7	1	$\{1/7, 2/7, 3/7, 4/7, 5/7, 6/7, 1\}$
2	5	2	$\{2/5, 4/5, 6/5, 8/5, 2\}$
3	6	3	$\{1/2, 1, 3/2, 2, 5/2, 3\}$
4	7	4	$\{4/7, 8/7, 12/7, 16/7, 20/7, 24/7, 4\}$
5	8	5	$\{5/8, 10/8, 15/8, 20/8, 25/8, 30/8, 35/8, 5\}$

TABLE II. Effective filling-factor sequences generated by parity-enhanced edge multiplicities for the representative sequence $(5, 6, 7, 7, 8, \dots)$, used for comparison with experimental fractional hierarchies.

n	ν_c	ν_n	Effective filling factors $\nu_{\text{eff}} = (\nu_p/\nu_c)\nu_n$
1	5	1	$\{1/5, 2/5, 3/5, 4/5, 1\}$
2	6	2	$\{1/3, 2/3, 1, 4/3, 5/3, 2\}$
3	7	3	$\{3/7, 6/7, 9/7, 12/7, 15/7, 18/7, 3\}$
4	7	4	$\{4/7, 8/7, 12/7, 16/7, 20/7, 24/7, 4\}$
5	8	5	$\{5/8, 10/8, 15/8, 20/8, 25/8, 30/8, 35/8, 5\}$

The second sequence listed above is used in the transport calculation shown in Fig. 7, where the resulting Hall resistance is compared directly with experimental data. Panel (a) displays the measured Hall resistance, while panel (b) shows the theoretical prediction obtained from boundary quantization with a weak parity-breaking interaction. In addition to the low-field plateaus, the high-field plateaus corresponding to fractions $3/7$ and $2/5$ are clearly reproduced. A perturbative analysis of zero counting in the presence of parity breaking is presented in Appendix E.

The theoretical predictions reproduce the experimentally observed integer and fractional plateaus at low, intermediate, and high magnetic fields with remarkable

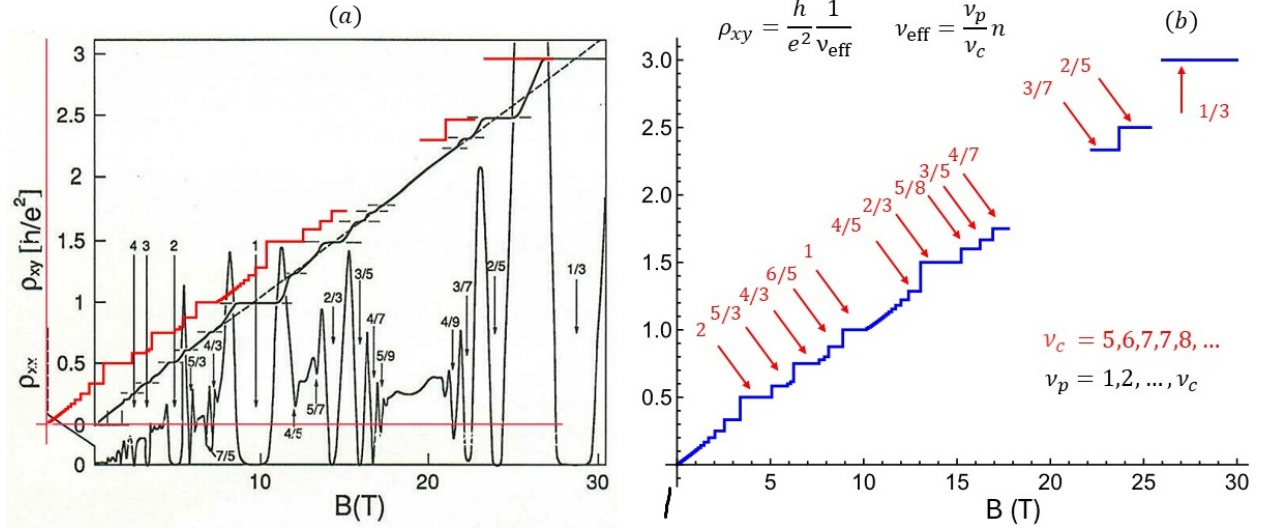


FIG. 7. Experimental and theoretical fractional Hall resistance based on boundary-quantized edge states with parity breaking. (a) Experimental Hall resistance $\rho_{xy}/(h/e^2)$ measured by Störmer *et al.* [12] (reproduced with permission from Elsevier). (b) Theoretical Hall resistance calculated within the present framework using Neumann boundary conditions and a weak parity-breaking parameter $b = 0.004$, for the Fermi energy $E_F = 0.001125\text{eV}$. The theoretical prediction (red curve) is overlaid on the experimental data to facilitate direct comparison. The prominent high-field fractional plateaus at $2/5$ and $3/7$ observed experimentally are reproduced by the theory.

accuracy, without invoking disorder, spin splitting, or phenomenological localization mechanisms, and within a single, unified boundary-based framework.

Geometric loci of boundary- and parity-generated sequences The multiplicity sequences produced by boundary quantization and their modification under parity breaking can be represented geometrically in the parameter space defined by the parity-breaking strength b and the lateral confinement scale L_y . Figure 8 shows the loci associated with representative fractional sequences obtained by imposing the boundary conditions on the Landau wave packets and counting the corresponding zeros, as described in Appendix D.

For a fixed magnetic field, the allowed edge spectra are determined jointly by the confinement length L_y and the parity-breaking parameter b . Each point in the (b, L_y) plane corresponds to a specific multiplicity of low-energy edge channels and therefore to a well-defined sequence of effective filling factors. The geometric curves shown in Fig. 8 identify the regions of parameter space where a given sequence is realized and remains stable under small variations of b and L_y .

In this representation, fractional plateaus do not arise as isolated numerical coincidences but as organized families of edge-state spectra. Sequences responsible for plateaus such as $1/3$, $2/3$, $2/5$, $3/5$, and $3/7$ occupy distinct but partially overlapping domains of the (b, L_y) space. Transitions between these domains correspond to changes in the number of boundary-supported edge branches and therefore to reorganizations of the effective filling-factor hierarchy.

The geometric picture also clarifies the complementary roles of boundary quantization and parity breaking. In the limit $b \rightarrow 0$, the loci reduce to those generated purely by Neumann and Robin boundary conditions, and the corresponding sequences coincide with the boundary-only hierarchy discussed above. As b increases, the loci deform and new families of fractional sequences appear, reflecting the enhanced multiplicity of low-energy edge states. Parity breaking therefore acts as a continuous control parameter that shifts the system between boundary-dominated and parity-enhanced regimes without altering the underlying Landau quantization.

This geometric organization explains the coexistence of several fractional plateaus within the same magnetic-field interval. For example, the $1/3$ plateau can occur both in wide samples with weak parity breaking and in narrower samples where parity-enhanced edge multiplicities are present, while fractions such as $2/5$ and $3/7$ emerge predominantly in regions where parity breaking increases the density of admissible edge states. The observed hierarchy of fractional plateaus is thus mapped onto a structured landscape in the (b, L_y) plane.

When the sequences identified in Fig. 8 are incorporated into the transport calculation, the resulting Hall resistance reproduces the experimental high-field fractional plateaus shown in Fig. 7. The geometric loci therefore provide a unifying interpretation: they link the microscopic zero-counting procedure, the boundary-controlled edge multiplicity, and the macroscopic transport signatures observed in the fractional quantum Hall regime.

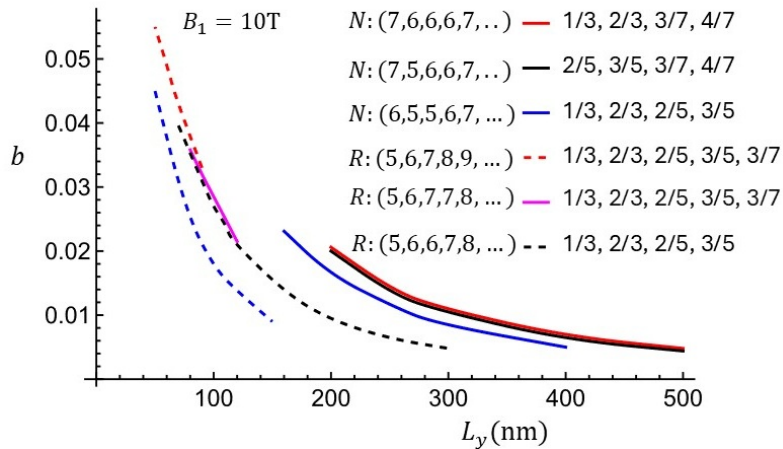


FIG. 8. Neumann and Robin multiplicity sequences and their geometric loci as functions of b and L_y . Given the magnetic field B_1 at which the plateau for $n = 1$ occurs, and choosing b and L_y , imposing the boundary conditions on the Landau wave packets η_y , and counting the number of zeros as described in the text and Appendix D, one obtains a sequence of effective filling factors. Searching for the same sequence in neighboring points of the parameter space (L_y, b) determines the geometric locus associated with each sequence of filling factors. The figure shows the loci corresponding to sequences responsible for fractional plateaus such as $1/3$, $2/3$, $2/5$, $3/5$, $3/7$, etc., at high magnetic fields.

VI. DISCUSSION AND CONCLUSIONS

The analysis developed in this work establishes a unified microscopic picture of quantized Hall transport in laterally confined two-dimensional electron systems by making explicit the role of boundaries in shaping the edge spectrum. Rather than treating edge states as secondary to bulk topology or as phenomenological transport channels, the present analysis shows that physically imposed boundary conditions directly determine the discrete structure, multiplicity, and occupancy of chiral edge modes. Transport quantization then follows from the propagation of these boundary-quantized states.

Within this picture, the quantum Hall effect emerges from the interplay of three interconnected elements. Bulk Landau quantization defines the existence and chirality of edge modes. Boundary conditions discretize guiding-center positions and longitudinal momenta, generating a structured hierarchy of edge channels. Phase-coherent transport through these channels produces the macroscopic Hall plateaus observed experimentally. This hierarchy provides a direct microscopic bridge between Landau quantization and the transport spectrum in real devices.

A central outcome of the theory is that physically consistent boundary conditions – Dirichlet, Neumann, and mixed (Robin-type) – lead to closely related edge localization patterns while differing in their allowed degeneracies and channel multiplicities. Boundary quantization alone accounts for the dominant integer Hall sequence and for several structured fractional features at low and intermediate magnetic fields. In this regime, quantization reflects the discrete spectrum of boundary-supported chiral modes rather than the global filling of bulk Landau levels alone.

At higher magnetic fields, a complete description requires incorporating a weak parity-breaking contribution associated with Hall-induced asymmetry, structural imbalance, tunneling, and unequal edge transmission. This controlled symmetry breaking reorganizes the low-energy edge spectrum without altering the underlying Landau-level ordering. When combined with Neumann or Robin boundary conditions, it enhances the multiplicity of low-index edge states and generates extended families of fractional filling factors. The fractional hierarchy thus arises from a boundary-driven reorganization of transmitting channels rather than from a modification of the bulk quantization itself.

From this perspective, bulk topology guarantees the existence and robustness of chiral edge modes, but the quantitative spectrum and multiplicity of those modes are determined by confinement and boundary physics. The effective filling factors measured experimentally correspond to the number of boundary-allowed and energetically populated chiral channels. Disorder and interactions, while important in real materials, act primarily as modifiers of an already quantized boundary spectrum rather than as the primary origin of quantization.

A key microscopic feature revealed by this analysis is the persistence of low-energy edge branches below the Fermi level even after the associated bulk Landau levels have crossed it. These long-lived boundary states maintain the continuity of the chiral current as the magnetic field varies and provide a geometric mechanism for the formation and evolution of Hall plateaus. Broad plateaus correspond to dense families of persistent edge modes, whereas narrower structures arise from higher-order branches with larger energy separations. The cascade of fractional plateaus

beyond the first integer plateau therefore reflects the sequential survival and depopulation of boundary-quantized channels.

Within this unified microscopic description, the integer and fractional quantum Hall effects appear as complementary manifestations of the same underlying mechanism: confinement-induced quantization of edge spectra refined by weak parity breaking. The quantized Hall resistance,

$$\rho_{xy} = \frac{h}{e^2 \nu_{\text{eff}}}, \quad \nu_{\text{eff}} = \frac{\nu_p}{\nu_c} \nu_n, \quad (49)$$

directly encodes the boundary-induced discretization of the transmitting edge structure and provides a compact analytical connection between microscopic spectra and macroscopic transport.

Beyond unifying the integer and fractional regimes, this approach establishes a general microscopic foundation for quantized transport in confined electronic systems. Because it relies only on geometric confinement, boundary-induced spectral discretization, and coherent edge propagation, its principles extend naturally to a broad class of materials in which boundary symmetries and confinement play a decisive role, including graphene, semiconductor heterostructures, topological insulators, and moiré systems.

More broadly, the present results clarify the relationship between topology and microscopic confinement in quantum Hall physics. Topological arguments ensure the robustness and chirality of edge transport, whereas boundary conditions determine the spectral structure through which quantization is realized. By explicitly connecting boundary physics, edge spectra, and transport, the theory bridges the gap between bulk invariants and the experimentally observed hierarchy of Hall plateaus.

This boundary-centered perspective opens several directions for future work. Extensions to interacting systems, nonuniform confinement, and time-dependent driving may reveal additional spectral reorganizations of edge channels. Likewise, engineering boundary conditions through electrostatic gating or nanostructuring offers a route to tailoring edge multiplicities and transport quantization in designed quantum devices. The analysis presented here therefore provides not only a unified interpretation of quantum Hall phenomena but also a basis for exploring boundary-controlled quantization in a wide range of quantum materials and mesoscopic systems.

Appendix A: Robin boundary condition and curvature constraint for Landau wave functions

We consider the general Robin boundary condition imposed at the sample edges,

$$\left(a \eta(y) + \frac{\partial \eta(y)}{\partial y} \right) \Big|_{y=\pm L_y/2} = 0, \quad (A1)$$

where a is a real parameter specifying the effective boundary constraint.

A basic physical requirement for a laterally confined system is the absence of probability flow normal to the boundary. The normal component of the quantum probability current density is

$$j_n \propto \Im \left[\eta^*(y) \frac{\partial \eta(y)}{\partial y} \right]. \quad (A2)$$

Since the transverse Landau functions $\eta(y)$ can be chosen real in the present gauge, the Robin condition (A1) guarantees that $j_n = 0$ at $y = \pm L_y/2$. Robin boundary conditions are therefore fully consistent with confinement at the sample edges.

To express Eq. (A1) in the Landau basis, we introduce the dimensionless coordinate ξ defined in Eq. (11), with boundary values $\xi_{\pm} = \xi|_{y=\pm L_y/2}$. Using the Gauss–Hermite form of Landau wave functions, the Robin constraint becomes

$$2n H_{n-1}(\xi_{\pm}) = (\xi_{\pm} - a) H_n(\xi_{\pm}), \quad (A3)$$

and, by iteration,

$$2n 2(n-1) H_{n-2}(\xi_{\pm}) = (\xi_{\pm} - a)^2 H_n(\xi_{\pm}). \quad (A4)$$

The second derivative of the transverse wave function can be written as

$$\frac{\partial^2 \eta(y)}{\partial y^2} = \frac{e^{-\xi^2/2}}{\ell_B^2} \left[(\xi^2 - 1) H_n(\xi) - 2\xi 2n H_{n-1}(\xi) + 2n 2(n-1) H_{n-2}(\xi) \right]. \quad (A5)$$

Evaluating Eq. (A5) at the boundaries and substituting Eqs. (A3)–(A4) yields

$$\frac{\partial^2 \eta(y)}{\partial y^2} \Big|_{y=\pm L_y/2} = \frac{e^{-\xi_{\pm}^2/2}}{\ell_B^2} (a^2 - 1) H_n(\xi_{\pm}). \quad (A6)$$

Equation (A6) shows that Robin boundary conditions impose a well-defined curvature of the transverse wave function at the sample edges. In particular, for the special values $a = \pm 1$ one obtains

$$\eta''(\pm L_y/2) = 0,$$

independently of the Landau index n (except at accidental nodes $H_n(\xi_{\pm}) = 0$).

In this work we focus on the special Robin boundary condition with $a = 1$. This ‘‘curvature-matching’’ constraint provides a physically transparent interpolation between Dirichlet and Neumann conditions while preserving zero normal current at the sample edges.

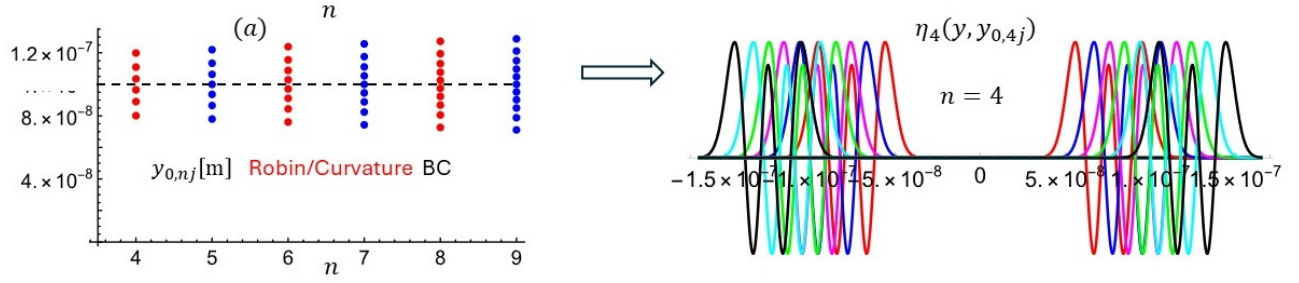


FIG. 9. Guiding-center quantization under Robin boundary conditions. (a) Discrete guiding-center positions $y_{0,nj}$ selected by the Robin constraint, Eq. (10). Right column: corresponding Landau wave packets evaluated at these quantized guiding centers for $n = 4$. Robin boundary conditions generate edge-localized branches closely analogous to the Dirichlet and Neumann cases (Fig. 1), but with two additional boundary-admissible solutions appearing near the inflection-point region of the Gaussian envelope of the Landau wave packet. Parameters: $B = 15$ T and $L_y = 0.2 \mu\text{m}$.

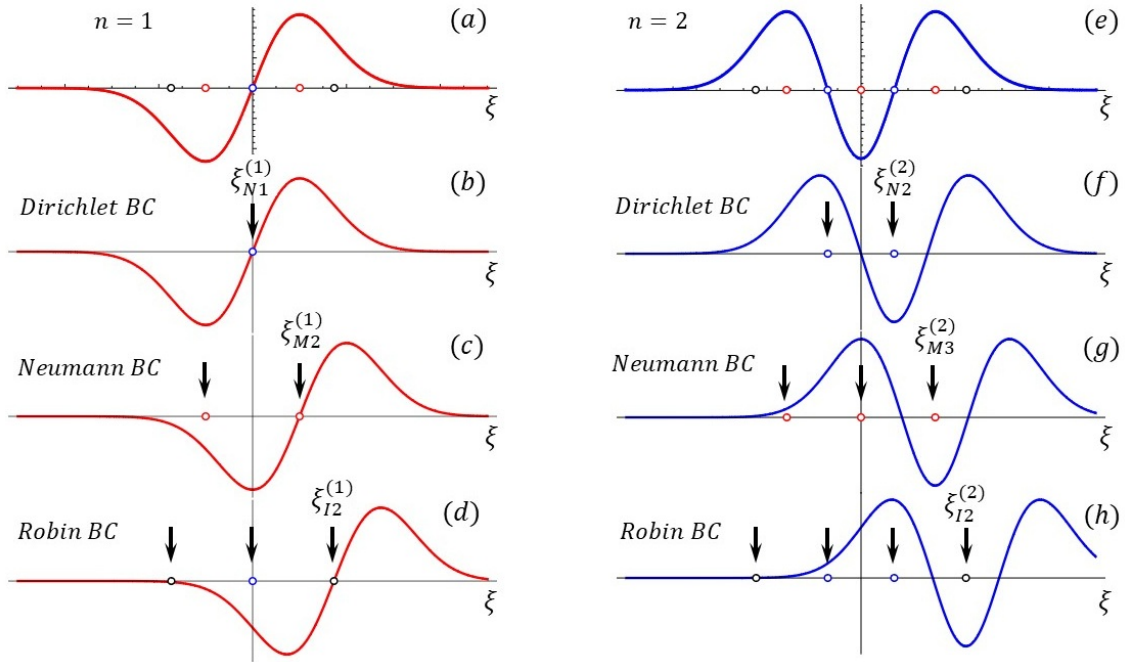


FIG. 10. Landau wave packets and the geometric meaning of Dirichlet, Neumann, and Robin boundary conditions. Left column: $n = 1$; right column: $n = 2$. Top panels show the Gauss–Hermite Landau wave packet $\eta_n(\xi) \propto e^{-\xi^2/2} H_n(\xi)$ together with its characteristic critical points: nodes (Dirichlet zeros, blue), extrema (Neumann zeros, red), and outer inflection points that generate additional Robin-admissible solutions (black). Second row: wave packets evaluated at the guiding-center positions (ξ_{N1}, ξ_{N2}) , admitted by Dirichlet boundary conditions at the sample edge, illustrating that Dirichlet constraints pin guiding centers to the nodes of η_n . Third row: corresponding Neumann-admissible guiding centers $(\xi_{M1}, \xi_{M2}, \xi_{M3})$, which coincide with the extrema of η_n . Bottom row: Robin-admissible guiding centers for the special condition $\pm \eta_n + \eta'_n = 0$, which includes both node-like solutions and two additional solutions $(\xi_{I1}$ and $\xi_{I2})$, near the outer inflection (turning-point) region of the wave packet.

Appendix B: Physical meaning of Dirichlet, Neumann, and Robin boundary conditions

In conventional one-dimensional quantum wells, Dirichlet, Neumann, and Robin boundary conditions are often interpreted as describing “hard” or “soft” confining walls that suppress the wavefunction at the boundaries and produce strong level repulsion. For Landau quantization

in a magnetic field, this interpretation is fundamentally misleading. The boundary conditions do not confine the wavefunction in the usual sense, do not truncate its Gaussian tails outside the nominal sample region, and do not generate the infinite-well type of level spacing. Instead, their essential role is to quantize the admissible guiding-center positions of displaced Landau wave packets.

1. Landau wave packets and boundary zeros. To clarify the microscopic action of boundary conditions, it is useful to express the transverse Landau eigenfunctions in terms of the dimensionless variable ξ defined in Eq. (11),

$$\eta_n(\xi) \propto e^{-\xi^2/2} H_n(\xi), \quad (\text{B1})$$

which has the form of a Gauss–Hermite wave packet. For each Landau index n , this structure possesses n nodes, $n + 1$ local extrema, and two outer inflection points associated with the Gaussian envelope.

These characteristic points acquire a direct boundary interpretation. Dirichlet boundary conditions,

$$\eta_n(\pm L_y/2) = 0, \quad (\text{B2})$$

select guiding centers located at the nodes of η_n , i.e., at the n real zeros of the Hermite polynomial H_n . Neumann boundary conditions,

$$\eta'_n(\pm L_y/2) = 0, \quad (\text{B3})$$

instead select guiding centers at the extrema of the Gauss–Hermite packet, corresponding to the $n + 1$ real zeros of η'_n .

More generally, Robin boundary conditions take the form

$$(a\eta_n + \eta'_n)|_{y=\pm L_y/2} = 0, \quad (\text{B4})$$

where a is a real boundary parameter. In this work we focus on the curvature-matching choice $a = \pm 1$, which is equivalent to the second-derivative constraint discussed in the preceding subsection. For this special case, the Robin condition yields the Dirichlet node spectrum together with two additional admissible solutions located near the outer inflection region of the Landau wave packet, producing $n + 2$ guiding-center roots.

These correspondences are illustrated in Fig. 10, where the nodes (Dirichlet), extrema (Neumann), and inflection-related roots (Robin) are marked explicitly for the lowest Landau levels. Evaluating η_n at these boundary-selected points shows that the guiding center is discretized precisely by the zeros of the imposed boundary constraint.

2. Guiding-center quantization without confinement. The Landau eigenstates in a finite Hall bar are displaced harmonic-oscillator wave packets,

$$\eta_n(y, y_0) \propto H_n\left(\frac{y - y_0}{\ell_B}\right) e^{-(y - y_0)^2/2\ell_B^2}, \quad (\text{B5})$$

whose maxima are centered at the guiding coordinate y_0 . The boundary condition does not restrict the spatial extent of these states. Rather, it imposes a linear constraint at $y = \pm L_y/2$ that selects a discrete set of admissible guiding centers $\{y_{0,nj}\}$.

A crucial point is that for all such allowed values, the corresponding Landau wavefunctions retain substantial weight outside the nominal interval $|y| \leq L_y/2$. As shown

in the right-hand panels of Figs. 1 and 9, approximately half of the probability density lies beyond the geometric sample edges, independent of whether Dirichlet, Neumann, or Robin constraints are imposed. Thus, boundary conditions in the quantum Hall problem do not act as confining walls; instead, they generate a discrete guiding-center spectrum that underlies edge-state quantization.

3. Absence of barrier repulsion. In an ordinary infinite square well, hard walls produce a characteristic repulsion of eigenvalues, with level spacings that grow with energy. No analogous effect occurs for Landau states in a magnetic field. As shown in Figs. 1 and 9, the guiding-center spectra selected by Dirichlet, Neumann, and Robin boundary conditions form nearly uniformly spaced sets, with no systematic repulsion from the edges.

This reflects the fact that the kinetic spectrum remains purely Landau-like, while the boundary conditions act only as linear constraints selecting admissible values of the guiding coordinate y_0 , without introducing an additional confining potential.

4. Same density, different multiplicity. For a fixed Landau index n , Dirichlet boundary conditions yield n admissible guiding centers, Neumann conditions yield $n + 1$, and the special Robin condition considered here yields $n + 2$. Despite these differences in multiplicity, Figs. 1(a)–(b) and Fig. 9(a) show that the *spacing* and *density* of the allowed $y_{0,nj}$ values are essentially the same in all three cases.

The additional Neumann solution corresponds to a parity-protected root of the derivative constraint and provides the microscopic origin of an extra edge branch that survives under weak asymmetry. The two additional Robin solutions arise near the outer inflection region of the Gaussian envelope, where the wave packet changes curvature. These extra boundary-allowed branches enrich the effective edge-channel counting and generate fractional filling-factor sequences.

5. Nearly identical edge wave packets. The right-hand panels of Figs. 1 and 9 display representative edge-localized Landau states (here for $n = 4$) evaluated at the quantized guiding centers obtained from Dirichlet, Neumann, and Robin conditions. In all cases the resulting states exhibit the same rapidly oscillating, edge-localized Gauss–Hermite structure, comparable leakage beyond the nominal sample boundary, and similar decay lengths.

Thus, the boundary condition does not modify the physical shape of an edge state; it determines only *how many* such boundary-consistent edge branches exist.

Summary. Dirichlet, Neumann, and Robin boundary conditions should not be interpreted as hard or soft confining walls for Landau wave functions. Rather, they serve as microscopic quantization rules for the guiding-center coordinate of displaced Landau wave packets. Their primary physical consequence is the boundary-dependent multiplicity of longitudinal edge-state channels: n for Dirichlet, $n + 1$ for Neumann, and $n + 2$ for Robin.

This boundary-controlled channel counting underlies the emergence of both integer and fractional Hall plateau

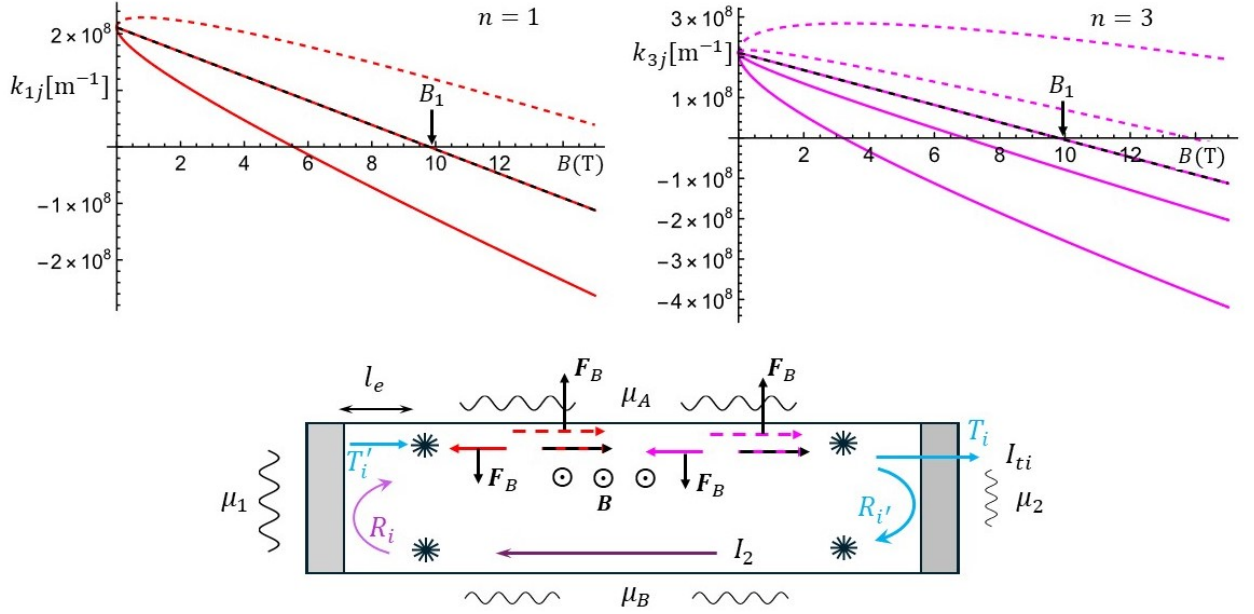


FIG. 11. Evolution of the longitudinal momenta $k_{x,nj}$ of boundary-quantized edge channels with magnetic field B . Solid colored curves show representative branches for different Landau indices n . Dotted curves denote the *pinned* edge states that remain localized near the upper boundary and continue to carry the chiral current as B increases. Dashed black curves (overlaid in color for each n) correspond to the $\xi_{nj} = 0$ solutions, which are purely kinetic and provide the reference momentum scale for the localized channels. A change in the sign of $k_{x,nj}$ indicates that the corresponding state exchanges from one edge to the opposite one, reversing its propagation direction on a given boundary while preserving the overall chirality of the system. The field $B_1 = 9.8$ T marks the onset of the $n = 1$ plateau. Parameters: $m^* = 0.067 m_e$, $E_F = (3/2)\hbar\omega_{c1}$ with $\omega_{c1} = eB_1/m^*$, and effective stripe width $L_y = 28.3896$ nm at B_1 .

sequences. In particular, Neumann and Robin conditions support additional edge branches that remain robust under weak parity breaking and give rise to the enriched fractional hierarchy observed experimentally.

Appendix C: Momentum sign, localization, and edge exchange

Figure 11 shows the longitudinal momenta $k_{x,nj}$ of representative boundary-quantized edge channels as functions of the magnetic field. Both the sign and magnitude of $k_{x,nj}$ carry direct physical meaning: for states localized near the upper boundary, positive k_x corresponds to propagation along the chiral direction of that edge.

The pinned low-energy channels identified in our analysis are characterized by large positive k_x and remain tightly localized near the physical boundary as the magnetic field increases. These modes therefore persist as robust conduits that sustain the edge current across successive Landau-level crossings.

In contrast, branches whose longitudinal momentum decreases in magnitude or changes sign progressively shift away from a given edge and effectively exchange to the opposite boundary. Such modes no longer contribute to transport on the original edge, but instead reappear as

counterpropagating channels on the other side of the Hall bar. The momentum evolution in Fig. 11 thus provides a microscopic picture of the *edge-exchange* mechanism. As the magnetic field varies, the roots of the boundary quantization conditions, parametrized by the guiding-center coordinates ξ_{nj} , shift continuously, reassigning localization and momentum between the two edges while conserving the total number of available edge-state channels.

This process preserves the global chiral structure of edge transport and clarifies why only a subset of parity-split channels remains energetically accessible and current-carrying in the fractional regime.

Appendix D: Counting zeros in the presence of parity breaking

As discussed in the main text, the number of conducting edge-state channels ν_c plays a central role in determining the effective filling factors that enter the transport problem. In the absence of parity breaking, ν_c is fixed uniquely by the imposed boundary condition—Dirichlet (DC), Neumann (NC), or Robin (RC). When a weak parity-breaking interaction is present, however, the number of admissible edge channels becomes a function of both the asymmetry strength b and the geometric ratio L_y/ℓ_B .

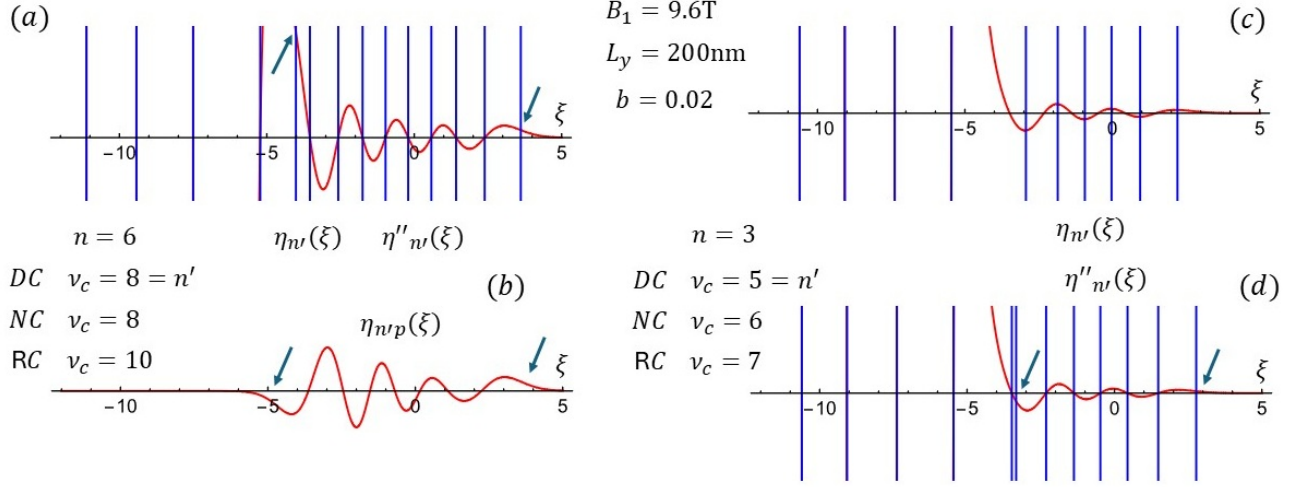


FIG. 12. Identification of Dirichlet (DC), Neumann (NC), and Robin (RC) admissible zeros in the presence of parity breaking. Shown are exact parity-broken solutions $\eta_{n'}(y)$ of Eq. (18) together with their third-order perturbative approximations $\eta_{n'p}(y)$ for $B_1 = 9.6$ T, $L_y = 200$ nm, and $b = 0.02$. Panels (a,b) correspond to $n = 6$, while panels (c,d) correspond to $n = 3$. Red curves denote the wave functions, and blue curves their second derivatives. Arrows mark inflection points where $\eta_{n'}''(y) = 0$ with $\eta_{n'}(y) \neq 0$, which determine the additional Robin-admissible roots. Panel (c) illustrates Neumann zeros ($\eta_{n'}' = 0$), while panel (d) shows Dirichlet zeros ($\eta_{n'} = 0$) together with the outer Robin roots. This inflection-point criterion provides a robust graphical method for counting conducting edge channels in the parity-broken case.

The exact solutions of the parity-broken Schrödinger equation, Eq. (18), are given in Eq. (19) in terms of parabolic cylinder functions. These generalize the Landau eigenstates and are naturally labeled by a continuous index n' , which provides only an approximate indication of the number of admissible boundary roots. A reliable determination of the Dirichlet, Neumann, and Robin zeros therefore requires a more direct criterion.

In practice, a brute-force numerical root search is cumbersome, since symbolic solvers return many closely spaced solutions. Instead, we employ a graphical method based on the structure of the wave packet and its derivatives, supported by a perturbative representation of the parity-broken states.

Figure 12 compares the exact wave functions $\eta_{n'}(y)$ with their third-order perturbative approximations $\eta_{n'p}(y)$, together with their second derivatives. Although third-order perturbation theory does not reproduce the full amplitude of the exact solutions, it accurately captures the location of the outer inflection points, which provide the relevant Robin-admissible roots.

For the Robin condition in the parity-broken case, the additional admissible zeros are identified by inflection points satisfying $\eta_{n'}''(y) = 0$ while $\eta_{n'}(y) \neq 0$. For $n = 6$ [panels (a,b)], the arrows mark precisely these inflection-point solutions, which coincide with the outer Robin roots. For $n = 3$, panel (c) illustrates the Neumann zeros defined by $\eta_{n'}'(y) = 0$, while panel (d) shows the Dirichlet zeros together with the corresponding outer Robin solutions.

Once these inflection points are identified, the number of Dirichlet, Neumann, and Robin admissible roots—and

therefore the number of conducting edge channels ν_c —can be determined unambiguously in the parity-broken regime.

Appendix E: Phase-space diagram of fractional states

The diversity of observed fractional quantum Hall plateaus is often described phenomenologically as a “zoo” of fractions. Within the present framework, however, these states can be organized into a structured hierarchy that reflects the interplay between boundary-selected guiding-center quantization and weak parity-breaking edge asymmetry.

Boundary conditions impose a discrete spectrum of admissible guiding centers and thereby fix the baseline multiplicity of edge-state channels within a given Landau level. The effective lateral width (L_y) controls the density of these boundary-allowed solutions, while a parity-breaking perturbation lifts the degeneracy between opposite edges and selectively reorganizes the channel counting. Together, $((L_y, b))$ define a natural parameter space in which different fractional filling factors correspond to distinct stable edge-channel configurations, as summarized schematically in Fig. 13.

Robust principal fractions—most notably ($\nu = 1/3$)—arise from top-tier configurations that persist over extended regions of this parameter space and are comparatively insensitive to microscopic sample details. By contrast, higher-order fractions emerge predominantly near the boundaries between competing admissible mul-

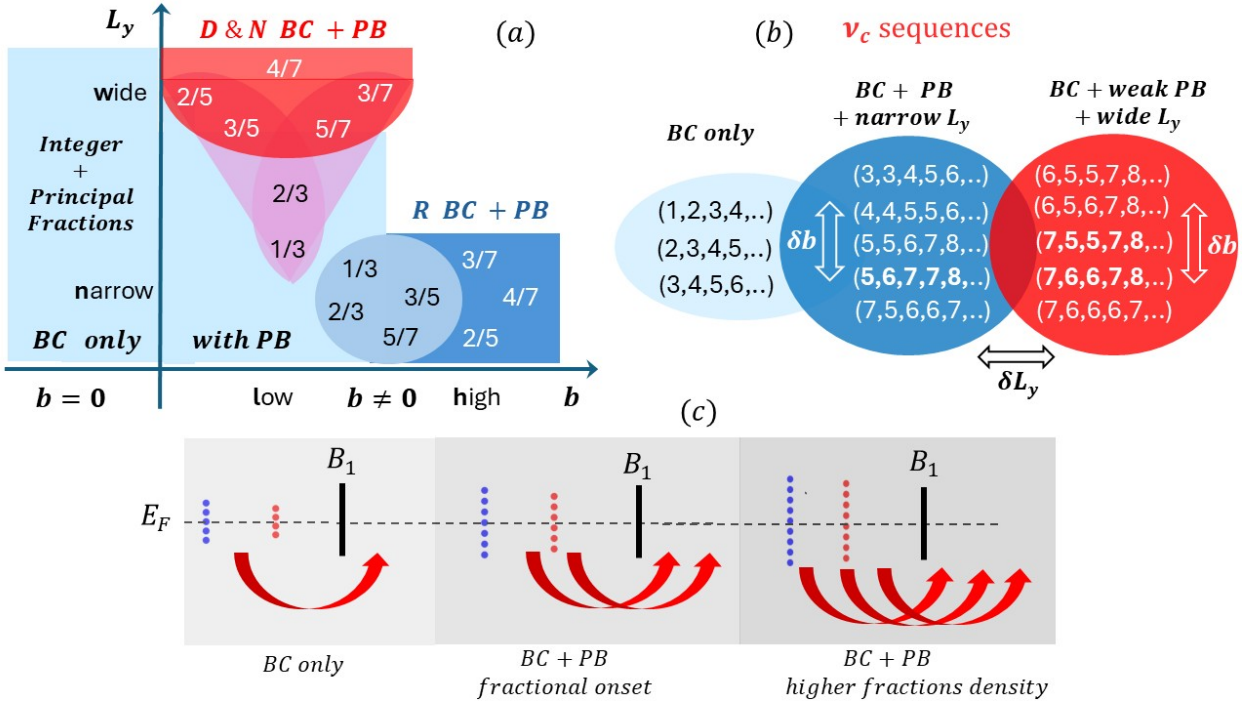


FIG. 13. Schematic phase space of fractional filling-factor sequences generated by boundary quantization and parity breaking. (a) Parameter map in the plane of effective lateral width L_y and parity-breaking strength b , identifying regimes in which Dirichlet/Neumann boundary conditions (upper region) or Robin boundary conditions (lower region) determine the admissible guiding-center solutions. The light-blue domain corresponds to integer and principal fractional states produced by boundary quantization alone. Boundary quantization sets the baseline multiplicity of edge channels, while parity breaking lifts the degeneracy between opposite edges and reorganizes the available branches. Principal fractions such as $\nu = 1/3$ remain stable over broad regions of parameter space, whereas higher-order fractions (e.g., $2/5$, $3/7$, $4/7$) appear only within restricted mixed domains. (b) Representative sequences of effective channel multiplicities ν_c in the boundary-condition-dominated, weak-parity-breaking, and wide-sample regimes, illustrating the sensitivity of subleading fractions to variations in b and L_y . (c) Emergence of edge channels pinned near the Fermi level for magnetic fields exceeding the $n = 1$ plateau field B_1 . Parity splitting selectively stabilizes subsets of chiral modes, increasing the density of accessible fractional plateaus at higher fields.

tiplicities. In this mixed regime, small variations in the parity-breaking strength (b) or in the effective width (L_y) can enable or suppress fractions such as $(2/5)$ or $(3/7)$, while leaving the dominant plateaus essentially unchanged.

This boundary-based organization provides a unified explanation for two coexisting experimental facts: the re-

markable reproducibility of the strongest fractional states and the pronounced sample dependence of weaker, higher-order plateaus. In this picture, the observed fractional hierarchy reflects how interaction-driven correlations are expressed within a guiding-center landscape that is filtered and structured by boundary quantization and edge asymmetry.

[1] von Klitzing K., Dorda G. & Pepper M. New Method for High-Accuracy Determination of the Fine-Structure Constant Based on Quantized Hall Resistance. *Phys. Rev. Lett.* **45**, 494 (1980)
 [2] Thouless, D. J., Kohmoto, M., Nightingale, M. P., & den Nijs, M. Quantum Hall Conductance in a Two-Dimensional Periodic Potential. *Phys. Rev. Lett.* **49**, 405-408 (1982).
 [3] Tsui, D.C., Störmer, L. & Gossard, A.C. Two-Dimensional Magnetotransport in the Extreme Quantum Limit *Phys. Rev. Lett.* **48**, 1559-1562 (1982).
 [4] Laughlin, R.B. Anomalous Quantum Hall Effect: An

Incompressible Quantum Fluid with Fractionally Charged Excitations *Phys. Rev. Lett.* **50**, 1395-1398 (1983).
 [5] Yu, R., Zhang, W., Zhang, H J., Zhang, S.C., Dai, X. & Fang, Z. Quantized Anomalous Hall Effect in Magnetic Topological Insulators *Science* **329**, 61-64 (2010).
 [6] McIver, J.W., Schulte, B., Stein, F.U., Matsuyama, T., Jotzu, G., Meier, G. & Cavallier A. Light-Induced anomalous Hall effect in graphene. *Nat. Phys.* **16**, 38-43 (2020).
 [7] Hastings, M. B. & Michalakis, S. Quantization of Hall Conductance for Interacting Electrons on a Torus. *Commun. Math. Phys.* **334**, 433-472 (2015).
 [8] Büttiker M., Absence of backscattering in the quantum

- Hall effect in multiprobe conductors *Phys. Rev. B* 38, 9375-9389 (1988).
- [9] P. M. Morse and H. Feshbach, *Methods of Theoretical Physics* (McGraw Hill, 1953), see page 679.
- [10] Koch, S., Haug, R.J., von Klitzing, K. & Razeghi, M. Observation of a spin-polarization instability in tilted magnetic fields. *Physica B* 184, 76-80 (1993).
- [11] Weis, J. & von Klitzing, K. Metrology and microscopic picture of the integer quantum Hall effect. *Phil. Trans. R. Soc. A* 369, 3954-3974 (2011).
- [12] Störmer, H.L. *Physica B* 177, 401-408 (1992).